A dynamic lithosphere-asthenosphere boundary near the equatorial Mid-Atlantic Ridge

Catherine A. Rychert[1*], Saikiran Tharimena[2], Nicholas Harmon[1], Shunguo Wang[3], Steven Constable[4], J. Michael Kendall[5], Petros Bogiatzis[1], Matthew R. Agius[6] and David Schlaphorst[7]

[1]*Ocean and Earth Science, National Oceanography Centre Southampton, University of Southampton Waterfront Campus, UK*

[2]*Faculty of Earth Sciences, Geography and Astronomy, University of Vienna, Austria*

[3]*Norwegian University of Science and Technology, Norway*

[4]*Scripps Institution of Oceanography, University of California, San Diego, San Diego, CA, USA*

[5]*Earth Sciences, University of Oxford, UK*

[6]*Department of Sciences, University of Roma Tre, Rome, Italy*

[7] *Instituto Dom Luiz (IDL), Faculdade de Ciências, Universidade de Lisboa, Campo Grande, 1749–016, Lisboa, Portugal*

ABSTRACT

In plate tectonic theory a weak asthenosphere is required to facilitate the motions of the rigid plates. Partial melt could weaken the mantle, in turn impacting convection, but to date the existence of persistent melt has remained controversial. A wide range of scenarios have been reported in terms of the location, amount and pathways of melt. Here we use

data collected by 39 ocean bottom seismometers deployed near the equatorial Mid-Atlantic Ridge on 0 to 80 Myr old seafloor. We calculate S-to-P (Sp) receiver functions and perform waveform modeling. We jointly interpret with shear-wave velocity tomography from surface waves and magnetotelluric (MT) imaging to take advantage of a range of resolutions and sensitivities and illuminate the structure of the oceanic lithosphere and the underlying asthenosphere. We image a tectonic plate thickness that increases with age in one location but undulates in another location. We infer thin and slightly thicker melt channels and punctuated regions of ascending partial melt several hundred kilometers off the ridge axis. This suggests melt persists over geologic timescales, although its character is dynamic, with implications for the lithosphere-asthenosphere boundary (LAB) and the driving forces of the plates. Ascending melt intermittently feeds melt channels at the base of the plate. The associated melt-enhanced buoyancy increases the influence of ridge-push in driving plate motions, whereas the channelized melt reduces the resistance of the plates to motion. Therefore, melt dynamics may play a larger role in controlling plate tectonics than previously thought.

Keywords: oceanic lithosphere-asthenosphere boundary, seismology, Mid-Atlantic Ridge, plate tectonics, receiver functions, melt dynamics

1. INTRODUCTION

1.1 MELT AND THE NATURE OF THE LITHOSPHERE ASTHENOSPHERE BOUNDARY

A large number of observations including imaging of sharp seismic discontinuities, strong electrical conductivity anomalies, slow seismic velocities and plate thicknesses that do not monotonically increase with age are inconsistent with a purely thermal definition for the tectonic plate (Forsyth et al., 1998; Kawakatsu et al., 2009; Key et al., 2013; Naif et al., 2013; Rychert et al., 2018b; Rychert and Shearer, 2009; Thybo, 2006). Several subsolidus mechanisms have been invoked to explain individual observations that do not conform to the classical thermal model of a plate (Beghein et al., 2014; Burgos et al., 2014; Cline et al., 2018; Karato et al., 2015; Yamauchi and Takei, 2016); although, each of these fails to universally explain all aspects of the aforementioned observations (Rychert and Harmon, 2018; Rychert et al., 2018b). Alternatively, partial melt may exist in the asthenosphere (Kawakatsu et al., 2009). Melt is expected to decrease the viscosity of the mantle (Hirth and Kohlstedt, 1995; Jackson et al., 2006), which could in turn influence mantle dynamics including the coupling of the plate to the deeper mantle and the thickness of the plate with potential implications for the driving forces of plate tectonics.

Despite its importance, constraining the amount, locations, and pathways of melt has proved challenging, especially near oceanic spreading centers where new plates are formed. Reports of melt are varied and come from different imaging techniques and locations. Shear velocities inferred from surface waves suggest melt exists over a broad area beneath the ridge, out to 400 km off-axis (Forsyth et al., 1998), whereas MT data suggests a narrow triangle, out to 20 km off-axis (Key et al., 2013). Seismic imaging from receiver functions, SS precursors, and approaches that include multiple S bounces implies sharp discontinuities that require melt beneath the plate over large swaths of the mantle (Gaherty et al., 1996; Kawakatsu et al., 2009; Rychert et al., 2018b; Tan and Helmberger, 2007), with a structure in which melt percentage gradually decrease with depth over tens of kilometers or more (Rychert and Harmon, 2018). Two seismic reflection surveys and one MT study imaged thin melt channels (Mehouachi and Singh, 2018; Naif et al., 2013; Stern et al., 2015) possibly caused by ponding along a permeability boundary (Sparks and Parmentier, 1991), although this has not been imaged everywhere (Key et al., 2013). Questions remain as to the exact geometry, location, volume, and pervasiveness of melt in the mantle and its relationship to the LAB.

Spreading rate is thought to be a key factor in determining the style of mantle flow, associated melting, and plate characteristics (Morgan et al., 1987; Parmentier and Morgan, 1990). However, to date much imaging of the mantle has been focused on the Pacific. For example, the fast-spreading East Pacific Rise (EPR) has been shown to be dominated by 2-D passive upwelling (Forsyth et al., 1998; Key et al., 2013), although an asymmetric sub-ridge anomaly (Forsyth et al., 1998) may also indicate additional influences such as across axis flow owing to lateral pressure or thermal gradients (Conder et al., 2002; Toomey et al., 2002), local melt buoyancy (Katz, 2010), or small scale convection (Harmon et al., 2011). Passive upwelling has also been inferred near the intermediate spreading Juan De Fuca and Gorda Ridges (Bell et al., 2016) but again with asymmetry suggesting additional influences, potentially the nearby Cobb hotspot. End member slow spreading at the Mid-Atlantic Ridge has not yet been investigated at a large scale and with a range of methods.

We installed 39 broadband ocean bottom seismometers and 39 ocean bottom MT instruments on and around the equatorial Mid-Atlantic Ridge, in the region of the Chain Fracture Zone from March 2016 to March 2017 (Fig. 1) (Harmon et al., 2020; Harmon et al., 2018; Wang et al., 2020). The deployment was part of the PI-LAB (Passive Imaging of the LAB) experiment, the EURO-LAB (Experiment to Unearth the Rheological Oceanic LAB), and the CA-LAB (Central Atlantic imaging of the LAB) experiment, to study a slow spreading ocean plate from its formation to an age of 80 Myr with a range of sensitivities and resolutions. Here we present new Sp receiver function imaging and waveform modeling of discontinuity structure (Rychert et al., 2018a). We jointly interpret with shear-wave velocity tomography from surface waves using teleseismic earthquakes and ambient noise (Harmon et al., 2020) and 2-D MT imaging (Wang et al., 2020) for a conceptual model of the dynamics of the region.

1.2 A BRIEF SUMMARY OF PREVIOUS MT AND SURFACE WAVE IMAGING RESULTS

Previous imaging in the PI-LAB study region revealed a thickening fast lid, several punctuated asthenospheric slow velocity zones and low resistivity anomalies, and also one fast and resistive asthenospheric anomaly (Harmon et al., 2020; Wang et al., 2020). Several MT anomalies are in good agreement with those inferred from surface waves. For instance, using the nomenclature of Harmon et al., (2020) and Wang et al., (2020), which we will continue to use here, high conductivity and slow seismic velocity at anomalies B, C, and F and high resistivity and fast seismic velocity at anomaly D as labelled for instance in Figure 1. The MT anomaly is shallower than the shear-wave anomaly inferred from surface waves at A, further west near B, thinner and broader than the shear-wave anomaly inferred from surface waves near F, and further west (shallower and deeper) near E. Seismic velocities need not match MT anomalies given that they have different sensitivities to the properties of the Earth. For instance, seismic waves are more sensitive to grain size and also seismic anisotropy caused by mineral alignment than MT. However, the locations of the anomalies are not discrepant given the resolutions of the methodologies (e.g., ~100 km lateral resolution, 10s km depth resolution for surface waves). General agreement between the models suggests temperature and melt, the factors that do impact both methodologies, are dominant (Harmon et al., 2020; Wang et al., 2020). Anomalies A, B and E are likely associated with sub-ridge upwelling and decompression melting. However, anomalies C and F are too far from the axis, to be ridge related, while anomaly D appears to be a lithospheric drip, and taken together suggest small scale convection. Receiver function imaging provides a means of testing the sharpness of the seismic LAB and provides further constraints on the character of melt at the base of the lithosphere that cannot be provided by shear-wave velocity based on surface waves alone.

2. Methods

2.1 RECEIVER FUNCTION IMAGING

We used seismic data from teleseismic events located at epicentral distances 55° to 80°. We considered all events with magnitude > 5.5. The data were rotated into P- and S-wave components using a transformation matrix for ocean bottom seismometers (Rychert et al., 2018a). For rotation of data, we used previously determined sediment velocities based on the P-to-S delay times from the sediment crust conversion and velocity-thickness relationships from previous work (Agius et al., 2018; Saikia et al., 2020). For stations where no P-to-S constraint or admittance constraint existed we used the linear interpolation between stations as reported in the P-to-S paper (Agius et al., 2018). We assumed a density of 2900 kg/m^3. The waveforms were bandpass filtered from 0.02 to 0.23 Hz. We tested a range of other bands. We found that the interpreted features persisted regardless of the exact band used. However, this band was most desirable in terms of the simplicity of the deconvolved waveforms. This band is also similar to that used in previous ocean bottom receiver function studies (Rychert et al., 2018a).

We visually inspected both the P- and S-wave components near the theoretical S-wave arrival on 3,319 waveforms. We selected waveforms with visible arrivals on the S-wave component, and with an S-wave amplitude larger than amplitudes before or after its arrival. Some energy was predicted on the P-wave component owing to conversions from the base of a sediment layer. We discarded waveforms where the apparent S-wave arrival was greater than 10 s off the theoretical arrival. We manually selected a window around the visible S-wave arrivals to use as the source waveform in deconvolution. After handpicking the data, we were left with 801 waveforms.

The data were deconvolved using an extended time multitaper method (Helffrich, 2006; Rychert et al., 2012) using a 50 s window, NW = 3, and 4 tapers (Shibutani et al., 2008). The deconvolved waveforms were inverted so that positive phases correspond to velocity increases with depth, consistent with polarity typical for P-to-S receiver functions. The waveforms were then migrated and stacked on a 0.5° x 0.5° grid, with a depth spacing of 1 km. For migration, we used a modified version of PREM to include estimated sediment properties (Agius et al., 2018; Saikia et al., 2020) and an oceanic crust of 7 km. In the crust we assumed a V_P/V_S ratio that varied with distance from the ridge from 2.0 to 1.77, to simulate the effect of near-ridge melt. In the mantle we assumed V_P/V_S ratio = 1.77. For stations with no sediment thickness information, we used the linear interpolation between stations, calculating V_S and V_P based on relationships from previous work as explained in the P-to-S study (Agius et al., 2018). We corrected for station elevations in the migration process and only used bins with more than three waveforms in the stack (Fig. 2). We smoothed the bins over the Fresnel zone of the waves with a minimum Fresnel zone cutoff of 50 km.

We tested the effect of a range of migration models. We tested using both P- and S-wave velocities from PREM (Dziewonski and Anderson, 1981), modified to include the sediment layer along with a 7 km crust. We also tested a constant crustal V_P/V_S ratio with distance from the ridge, the effect of using constant vs. varying sediment thickness, and also using a full 3D shear velocity model inferred from inversion of surface waves from this study and calculating the P-wave velocity, assuming a range of constant V_P/V_S ratios (1.77 – 2.0) and also varying them with distance. We also tested using PREM (Dziewonski and Anderson, 1981) and a range of V_P/V_S in the range of 1.77 to 2.0, i.e. an increase in P-wave velocity of 1.5 % to 14.5 % compared to PREM P-wave velocities.

The features interpreted here were present in all of these tests with variable degrees of clarity, suggesting that they are the robust features. In addition, there was no significant change in the discontinuity depths and/or the age-depth trend of the LAB phase. A 5% faster model causes discontinuities near 30 – 40 km depth to migrate 1 km shallower and vice-versa if slower velocities are assumed, while still maintaining the age-depth relationship of the LAB phase. However, if larger V_P/V_S is used at the ridge and lower V_P/V_S away from the ridge, the discontinuities beneath the ridge migrate shallower by ~2 – 3 km, enhancing the age-depth trend. Although phases at greater delay times/deeper depths have the potential to be more influenced by migration model choices, V_P/V_S variations beneath thicker, melt-free lithosphere are predicted to be less, making the overall expected effect moderate. We tested the potential impact of an inaccurate V_P/V_S assumption in the migration model by changing mantle V_P by 5%, which resulted in 5 km shifts in phases around 80 km deep. Therefore, we report error in the depth of the discontinuities as ± 5 km, encompassing modest migration model variations beneath older lithosphere and strong variations beneath younger lithosphere. We interpret phases that are significantly different from zero according to error bounds calculated for 95 % confidence (Fig. 3). We show the depth and locations of where we detected the LAB phase above the threshold of formal error in Fig. 2.

2.2 RECEIVER FUNCTION WAVEFORM MODELING

We modeled the receiver function waveforms at anomalies A, C, D, E, and F with synthetic seismograms, processing them in the identical way as the data. We modeled the receiver functions in two ways to illustrate the range of potential models that fit the data. We did not model anomaly B given that there is not a significant receiver function and the locations of the resistivity and shear-wave anomalies from surface waves are not spatially coincident, likely owing to variable resolutions of heterogeneous structures. Disambiguating complexity at anomaly B is beyond the scope of this study. We first forward modeled the data assuming a minimum parameterization, that included one Moho layer, one lithospheric layer and one asthenospheric layer. We allowed the layer thicknesses and shear velocities to vary. We also performed a discretized layer inversion using 10 km thick layers. We permitted shear velocity and Vp/Vs in the layers to vary between 3.8 - 4.8 km/s and 1.7 - 2.0, respectively, with the remaining assumptions the same as for the forward approach. We also tested a range of fixed V_P/V_S, although it did not impact our overall result, i.e., beyond our error bars. The minimum parameterization is appealing in that it provides the simplest solution. The discretized inversion illustrates the endmember case for smoother gradients. The approach could be considered an overparameterization. However, the results of the inversions were primarily simple gradient structures, which could instead be described by sharpness and magnitude rather than the velocities of each individual step without created unresolved degrees of freedom. Therefore, we use this approach to illustrate how smooth the gradients could be while still matching the data.

3. RESULTS

3.1 RECEIVER FUNCTION IMAGING RESULTS

Sp receiver functions image a velocity increase with depth at 4 – 8 km below the seafloor across the region associated with the Moho (Figs. 4). At greater depths Sp images a negative phase. Synthetic waveform modeling suggests it is consistent with a sharp velocity decrease of 6 – 15 % over < 30 km depth (see section 3.2). The depth of the velocity contrast increases monotonically with age in the western side of transect II in the south from 30 to 80 ± 5 km depth below sea level (Figs. 4, S1, S2). In the eastern side of transect II the negative phase is patchy. In transect I in the north the phase has more complex topography and is characterized by larger error and a patchy character (Figs. 2 - 4). The transects and therefore the interpretations are located in regions where the hit count is high, and therefore LAB detection vs. non-detection must be either real or an artefact of S-to-P resolution (Fig. 2), which we address in subsequent sections. We do not interpret features that are not significantly different from zero according to formal error and therefore, by definition they cannot be noise. In addition, the interpreted features are clearly present in the highest quality receiver functions and do not arise from noise (Fig. S1).

3.2 RECEIVER FUNCTION MODELING RESULTS

We find good fits to the receiver function waveforms using the minimum parameterization approach (Fig. 5). We find strong, sharp velocity drops at the LAB at anomalies A (8 % at 36 km), C (11 % at 43 km), E (13 % at 34 km) and F (15 % at 39 km). No negative LAB discontinuity is required to match the receiver functions at anomaly D. We do not attempt to fit additional phases by adding discontinuities, given that we limit the number of parameters, in particular the second negative peak at anomaly A. The additional peak could be real, representing continued drop in velocity or they could represent smearing of slightly different LAB depth in nearby bins, given strong nearby lateral variability (Fig. 4).

In the discretized approach, we find that we also fit the receiver function waveforms well. In this parameterization the LAB phase is explained by smoother velocity depth profiles that still include large velocity drops from the highest to the lowest velocity: A (12 % from 30 - 50 km depth), C (6 % at 40 km depth), E (11 % from 30 - 40 km depth), and F (13 % from 20 - 50 km depth). At anomaly D a broad and moderate velocity drop (7 % from 20 to 50 km depth) can also be included, while still fitting the data. At anomaly A the discretized inversion prefers a broad velocity gradient to produce a better match the second negative pulse, within the error bounds. However, we did not force a fit to within error given that the deeper pulse could be caused by lateral smearing of nearby topography on the gradient.

4. DISCUSSION

4.1 COMPARISON OF RECEIVER FUNCTIONS TO RESISTIVITY AND SHEAR-WAVE VELOCITIES FROM SURFACE WAVES

There is good agreement with the depth of the discontinuity beneath the western half of transect II and most other reported discontinuity depths from scattered waves and transect studies beneath the oceans unaffected by hotspot volcanism globally (Fig. 6). There is also agreement with the depths of the lowest velocities from surface waves from a global model across the Pacific (French et al., 2013). However, there are also regions that exhibit significant deviations, for instance beneath other areas of our study region and also beneath ocean islands or regions affected beneath hotspots. This suggests that while on average temperature plays a large role in dictating the thickness of the lithosphere, there are also important deviations (Rychert et al., 2020). Here we will explore these further.

There is good agreement between the presence of a significant negative receiver function phase and locations of underlying slow shear-wave velocity anomalies inferred from inversion of surface waves (< 4.2 km/s) at 50 – 100 km depth (Fig. 4, 5, 7 anomalies A C, E, and F) and also locations where moderate MT conductivities extend to greater depths, i.e., greater than a thin 10 km channel (Fig. 5 e.g., anomaly B, C, F, and just west of E). The negative receiver function phase is absent or insignificant from zero where the high velocity, high resistivity drip occurs (Fig. 5, 7 anomaly D), where the conductivity anomaly is a thin channel (Fig. 7 either side of anomaly F) and where the depth of the negative receiver function phase undulates, based on the punctuated shear-wave velocity anomalies from surface waves and MT anomalies (sections of transect I).

The relationship of the significant negative receiver function phases to the strong shear-wave anomalies from surface waves and moderate MT anomalies over broader depths is likely explained by differences in resolution. MT can resolve thin channels on the order of 10 km

(Parker and Whaler, 1981), whereas Sp suffers from destructive interference. For instance, the amplitude of conversions from the top of a 10 or a 5 km thick channel would be reduced to ~70 % and ~30 % of the original values, respectively, for the filtering used here (Rychert and Harmon, 2018), beneath the detectability threshold from our receiver function error analysis. Therefore, the locations where receiver functions clearly image a singular negative velocity discontinuity likely represent locations where low velocity zones exist over > 10 km depth, gradually increasing in velocity with depth.

The lack of significant negative receiver function phases adjacent to punctuated shear-wave velocity anomalies from surface waves and MT imaging is likely also explained by resolution. The shear-wave tomography based on local Rayleigh waves images near vertical edges to anomaly structures at 30 to 55 km beneath the ridge in transect I (Saikia et al., 2021). Sp cannot easily resolve dipping or undulating topography (Lekic and Fischer, 2017) (Fig. 7 transect I particularly near anomaly B).

In light of the different resolutions of the three approaches, the patchy receiver function imaging of negative discontinuities is expected. The association of the negative phase with the base of the seismically fast lithosphere from surface waves and the resistive lithosphere from MT imaging suggests it marks the LAB.

Overall, Sp LAB phases together with MT imaging and surface waves illuminate the structure of the lithosphere and the asthenosphere. In the western side of transect II, the plate thickens relatively monotonically with age (Fig. 4, 7, S2) and is characterized by a single velocity drop rather than a thin channel (drop followed by a deeper velocity increase) (see section 4.2 and Fig. 2, 7). In the eastern section of transect II the lithosphere is underlain by a channel that is thinner (~10 km) close to the ridge and extending to 10 - 15 Myr. Near anomaly F the channel is thicker (> 10 km), flatter, and gradually tapers with depth. In transect I the seismically fast and resistive plate undulates in thickness with age, and there is a single velocity drop in some regions, such as anomaly C. No channel is apparent.

4.2 1-D MODEL COMPARISONS AND RECEIVER FUNCTION MODELING

We compare the receiver functions to the surface wave and MT models in the locations of the discrete major asthenospheric anomalies. The 1-D profiles through anomalies A, C, E and F all show LAB receiver function peaks that are significant from zero. The depths of the peaks all fall within the gradual drops in shear-wave velocity with depth at the base of the plate (Fig. 4 - 6). Shear-wave velocities in the slow anomalies also reach as slow as 4.2 km/s or slower in the surface wave model. In contrast, at anomaly D no strong sharp phase is required by the receiver function and shear-wave velocities are fast (Vs > 4.4 km/s over the upper 150 km of the mantle) in the location of a hypothesized lithospheric drip. Anomaly A is slightly shallower in the MT imaging than the seismic, potentially owing to resolution. Anomaly B and C are muted in the receiver functions, which is likely explained by lateral variability in the depth of the phase, as evidenced by undulating contours from MT and surface waves. The overall agreement among the independent seismic methods for anomalies A, C, D, E and F gives us confidence in these features.

The exact shapes of the velocity profiles of the receiver function models and the shear-wave velocities inferred from surface waves are different at least for some anomalies and some parameterizations. While the best-fitting receiver function models fall outside the formal error bars on the shear-wave velocities inferred from surface waves, the two are not necessarily discrepant. The sensitivity kernels of the shear-wave velocities from surface waves (Harmon et al., 2020) mean that the inferred shear-wave velocities are smoothed over a depth range and the error bars represent uncertainty in the average over that depth range rather than uncertainty in the velocity at any single depth. Therefore, the shear velocity from surface wave modeling cannot be simply compared with the receiver function result at any single depth.

Overall, the modeling results provide a range of potential models that could fit the data. Anomalies A, C, E, and F all require strong, sharp velocity gradients: A (8 - 12 % over < 20 km), C (6 - 11 % over 0 km), E (11 - 13 % over < 10 km) and F (13 - 15 % over < 30 km). None can be explained by a purely thermal model such as half-space cooling or the plate cooling model which are characterized by broader velocity gradients (over > 40 km depth) beneath 0 - 30 Myr old lithosphere (Tharimena et al., 2017), none of which are predicted to produce a converted receiver function strong enough for interpretation (Rychert and Harmon, 2018). Of course, there are error bars on the data which might allow for smaller velocity drops, particularly for anomalies C and F. However, this would not be consistent with the shear-wave velocity model from surface waves, which overall shows very good agreement with the total drop from the receiver functions and requires absolute velocities < 4.2 km/s in the asthenosphere. This suggests that muted receiver function amplitudes and error bars at C and F are more likely a product of lateral variability of depth of the discontinuity, and sharp discontinuities inconsistent with a thermal model are required at anomalies A, C, E, and F.

4.3 COMPARISON OF LITHOSPHERE-ASTHENOSPHERE STRUCTURE

The sub-ridge lithosphere from receiver functions, surfaces waves, and MT imaging is thicker (20 – 25 km) than the non-existent plate beneath the fast spreading EPR (Harmon et al., 2009; Key et al., 2013), and equal to or thicker than the 20 km thick plate beneath the intermediate spreading ridges in Cascadia (Rychert et al., 2018a). This trend of thicker sub-ridge lithosphere for slower spreading rates is predicted for lateral conductive cooling (Morgan et al., 1987).

The high conductivity channel from MT is similar to some previous channels imaged north of our study area (Mehouachi and Singh, 2018) and beneath the Cocos (Naif et al., 2013) and Pacific Plates (Stern et al., 2015). However, it is dissimilar with the lack of a channel imaged, for instance, in the remainder of our study area and also near the EPR and Mohns Ridge (Baba et al., 2006; Forsyth et al., 1998; Johansen et al., 2019; Key et al., 2013).

The apparent extreme thickening, or drip-like feature at 30 Myr (Figs. 4 - 6, anomaly D) and also the punctuated anomalies off-axis (e.g., C and F) differ from the smooth, monotonic increases in plate thickness in the western side of transect II and as observed in the MELT experiment (Harmon et al., 2009) and Cascadia (Rychert et al., 2018a). Punctuated anomalies that are distant from the ridge axis are also different from the previously imaged singular, focused sub-ridge anomalies of other studies (Baba et al., 2006; Forsyth et al., 1998; Johansen et al., 2019; Key et al., 2013), although our study includes a variety of sensitivities and extends to ages 8 – 25 times older than these studies.

4.4 A DYNAMIC LITHOSPHERE-ASTHENOSPHERE SYSTEM

Several aspects of the observations are not consistent with a model that includes purely conductive cooling. The receiver function phases require sharp velocity gradients (6 – 15 % over < 30 km). Subtle negative receiver function phases can be produced for thermal models (Fischer et al., 2020; Rychert and Harmon, 2018), although these are smaller than the requirements of our observations. Therma gradients over the broadest 20 – 30 km depth ranges from our waveform modelling can only explains about a 4 % drop (Jackson and Faul, 2010). Similarly, the magnitudes of the high conductivity anomalies (< 1 Ω m) cannot be explained by and slow seismic velocities (Vs < 4.2 km/s), channels structures, and punctuated off-axis anomalies are not explained by thermal models (Harmon et al., 2020; Wang et al., 2020).

Several sub-solidus mechanisms have been proposed to explain observations that are discrepant from thermal models. Seismic anisotropy from the alignment of olivine does not affect MT data, and therefore can be excluded in all locations where the methods agree. Also, Rayleigh wave anisotropy using local events is generally small < 3% throughout the study area (Saikia et al., 2021), and associated impacts on seismic imaging would be very low (Rychert and Harmon, 2018). Near solidus temperatures can cause very low seismic velocities (Yamauchi and Takei, 2016), although this would not explain the MT imaging, and it is also likely that the mantle near a mid-ocean ridge system will be above the solidus temperature. Mantle oxidation may affect seismic waves (Cline et al., 2018), but this is expected to be low at mid-ocean ridges and therefore not likely a factor. In the elastically accommodated grain boundary sliding model an increase in the sharpness of the velocity gradient with age is predicted, which would cause larger amplitudes and/or more impulsive receiver function phases at older ages (Karato et al., 2015), but this is not observed. In addition, this model would not likely affect MT data. Finally, recent laboratory experiments suggest that water does not affect observed seismic wave velocities (Cline et al., 2018), and the amount of hydration required to explain the magnitude of the conductivity anomalies would necessarily mean that the mantle is partially melted (Key et al., 2013).

Alternatively, partial melt could explain the sharp decreases in seismic velocity with depth, the slowest seismic velocity anomalies, the lowest resistivities, and the channelized and punctuated anomaly structures. Slow shear-wave velocity anomalies inferred from surface waves were reported to be 1 – 3 % (Harmon et al., 2020) in comparison to experimental predictions for peridotite at asthenosphere conditions (Jackson and Faul, 2010). Comparison to receiver function profiles suggests general agreement in terms of the slowest asthenosphere velocities, but a sharper transition from the fast lithosphere to the slower asthenosphere, and therefore a locally more pronounced anomaly than predicted by experimental predictions for thermal models or resolvable by surface waves (Fig. 5). Therefore, we proceed considering the new tighter constraints on the strong sharp drop from receiver functions. The receiver functions require a velocity drop of 6 – 15%. A thermal gradient at the base of the plate could explain up to a 4 % velocity drop for the broader, 20 – 30 km, gradients of the discretized model corresponding to the larger velocity drops (Jackson and Faul, 2010), i.e., not the 6 % drop over 0 km at anomaly 6. Therefore, after accounting for the maximum effect of temperature we are left with a 6 – 11 % velocity drop. Assuming a 2.7% velocity reduction per 1% melt fraction for melt distributed in tubules (Hammond & Humphreys, 2000) or 2.0% velocity reduction per 1 % melt fraction assuming equilibrium melt geometries (e.g., Clark & Lesher, 2017), suggests melt fractions, 2.2 – 5.5 %. Alternatively, if melt exists in films it could result in an 7.9 % drop in velocity per 1% percent partial melt, suggesting melt fractions of 0.8 – 1.4 %. These estimates from receiver functions are in good agreement with the predicted melt fractions at the lower end of MT modeling which require 1 – 7 % melt (Wang et al., 2020). Considered together the seismic and MT results can be explained by 1 – 5.5 % melt.

Our observations suggest two different configurations for melt, both channelized at the base of the plate and distributed in distinct broad regions with length scales on the order of 100 km or more (Fig. 8). The melt channels are characterized by variability in the sharpness in the gradients in melt volume at their base. Seismic and MT imaging together suggests a thicker channel with gradual drop off in melt percentage with depth in the western side of transect II, a thinner, sharper channel (10 km or less) in most of the eastern side of transect II, a thicker channel with gradual drop off with depth in the vicinity of anomaly F, and the lack of a channel in transect I (see section 4.2).

The existence of melt with variable character is supported by recent geodynamic modeling with non-Newtonian viscosity and two-phase flow that produces ‘porosity waves’, ephemeral melt-rich pockets that rise from depth and become thicker and more closely spaced as they approach and pond beneath permeability boundaries at shallow depths (Sim et al., 2020). Our punctuated anomalies particularly in transect I (e.g., anomaly C) are consistent with rising melt. Whereas melt beneath the plate over a broad depth range (near anomaly E) and in a thin channel (west of anomaly F) in transect II could represent melt ponded beneath the plate. The lack of an imaged channel in transect I could imply the ponded melt in the region has left the system and has yet to be replenished. The difference in the character of the melt geometry between our two transects suggests that melt is dynamic, and we have imaged two different stages in the melt migration process.

Our observation of broadly distributed melt, far from the ridge axis requires another dynamic component to create upwelling, such as small-scale convection due to lithospheric instabilities (Richter, 1973). In these models, the earliest drips start beneath 5-30 Myr seafloor for cases with a low viscosity asthenosphere (~10^{17}-10^{18} Pa s) (Buck and Parmentier, 1986), in agreement with our observation. Alternatively, upwellings could be driven by mantle chemical heterogeneity. Broadly distributed melt will also lower mantle viscosity and further enhance asthenospheric convection. This could also explain why seafloor subsidence and heat flow are more muted than predicted beneath the oldest seafloor, > 70 Myr (Parsons and Sclater, 1977).

Our observations of melt in a variety of forms unify seemingly discrepant observations of melt channels at the base of the plates (Mehouachi and Singh, 2018; Naif et al., 2013; Stern et al., 2015), including the lack thereof (Key et al., 2013), and broadly distributed melt in the asthenosphere (Forsyth et al., 1998). It suggests melt is persistent over geologic timescales, yet dynamic in character. Since melt would decrease the viscosity of the mantle, it would also define the plate. Therefore, plate thickness and character, and lithosphere-asthenosphere coupling are highly dynamic, and dependent on melt dynamics. Episodic melt-enhanced buoyancy beneath the ridge could increase the influence of ridge-push in driving plate motions. In addition, melt channels at the base of the lithosphere would reduce its basal drag resistance. Enhanced melt buoyancy and also enhanced decoupling may be key to explaining divergent plate motions beneath the Atlantic in the absence of significant drivers from surrounding subducting slabs. Plate spreading may be further assisted by deep upwellings from the lower mantle beneath the Atlantic that have been proposed based on a thinned mantle transition zone (Agius et al., 2021). In addition, interplay between upwelling and channelizing could result in temporal variations in forcing, and explain observed plate velocity variability (Coli et al., 2014). Melt dynamics could play a larger role in controlling plate motions than previously thought. Understanding the role of melt generation and migration as a driving force will be needed for a complete understanding of plate tectonics.

5. CONCLUSIONS

We image the oceanic lithosphere and asthenosphere in the region near the equatorial Mid-Atlantic Ridge using Sp receiver functions. The LAB increases monotonically with age from 30 to 80 ± 5 km depth in one location, but the LAB is sporadically detected at 20 – 80 ± km depth in other regions. The locations of the LAB detections and depths are consistent with anomaly structures in the resistivity and surface wave-derived shear velocity models when the resolutions of the approaches are considered. The sharp LAB discontinuities (6 – 15 % over < 30 km depth), strong seismic (Vs < 4.2 km/s) and MT anomalies (< 1 Ω m), punctuated anomaly characters, and channel structures are not consistent with a purely thermal model. To explain the LAB discontinuities, seismic, and resistivity anomalies in the asthenosphere requires 1 – 5.5 % partial melt localized in upwellings and also ponded beneath the lithosphere. Small scale convection may explain off-axis melt supply. The observations of melt with variable character reconciles previous seemingly discrepant reports from different studies and suggests we have imaged two different stages of melt migration. Melt episodically rises from depth, ponds beneath the plate, and accumulates before eventually leaving the system. Since the presence of melt would define the plate, it suggests that the LAB is dynamic, varying according to mantle dynamics and melt generation and migration. Also, melt dynamics likely play a larger role in driving plate motions than previously thought, with melt buoyancy aiding ridge push and reduced viscosity enabling plate motions.

ACKNOWLEDGMENTS

We thank the captain and crew of the R/V Marcus Langseth and the RRS Discovery and also the scientific technicians. We thank K. Davis for assistance with the schematic in Fig. 8. C.A.R. and N.H. were funded by the Natural Environment Research Council (NE/M003507/1) (PI-LAB) and the European Research Council (GA 638665) (EURO-LAB). J.M.K. was funded by the Natural Environment Research Council (NE/M004643/1). S.C. was funded by the National Science Foundation under grant OCE-1536400 (CA-LAB). D.S. was supported by the Portuguese Science and Technology Foundation (FCT/Fundação para a Ciência e Tecnologia), under project PTDC/CTA-GEF/30264/2017 and UIDB/50019/2020 – IDL

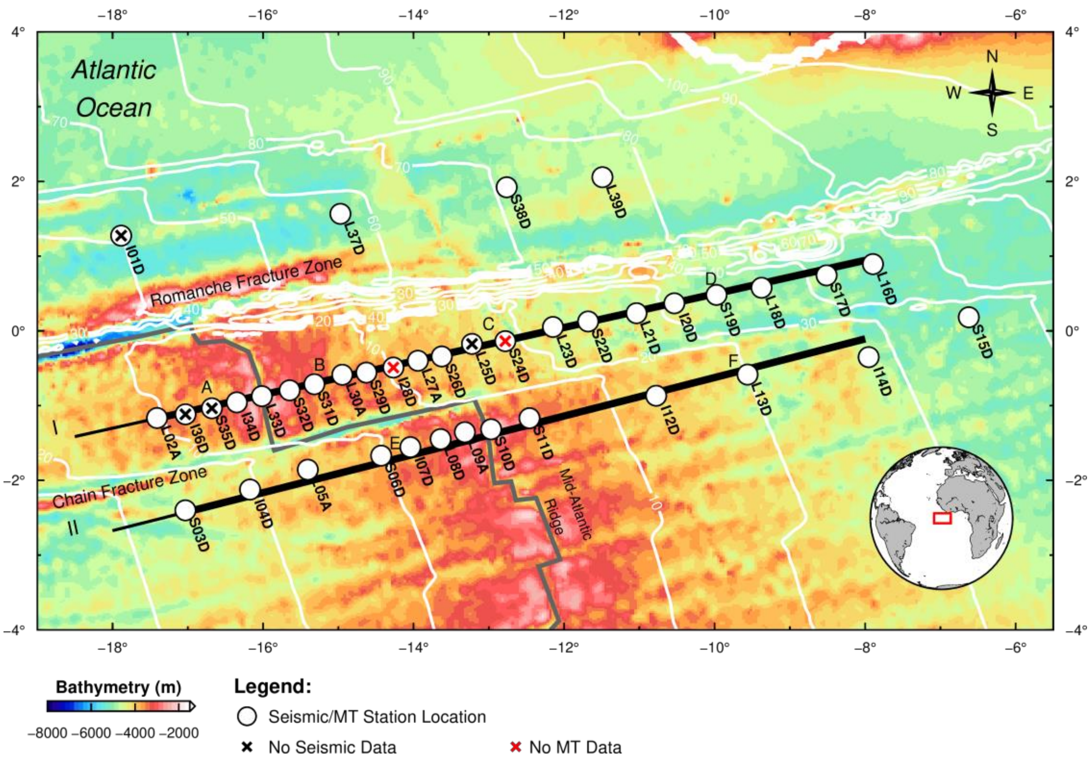

Figure 1

Map of study region. Background color shows bathymetry. Inset map shows global location. Large white circles show seismic and MT station locations. X's indicate locations where no data was used in the seismic (black) and MT (red) analysis. Dark grey line shows the plate boundary. White lines show age contours (in Myr) (Muller et al., 2008). Thick black lines indicate transect locations, I (northern) and II (southern), with slightly longer limits (thin black line) used in the shear-wave velocity and receiver function transects shown in Fig. 4. Anomaly locations are indicated by the capital letters.

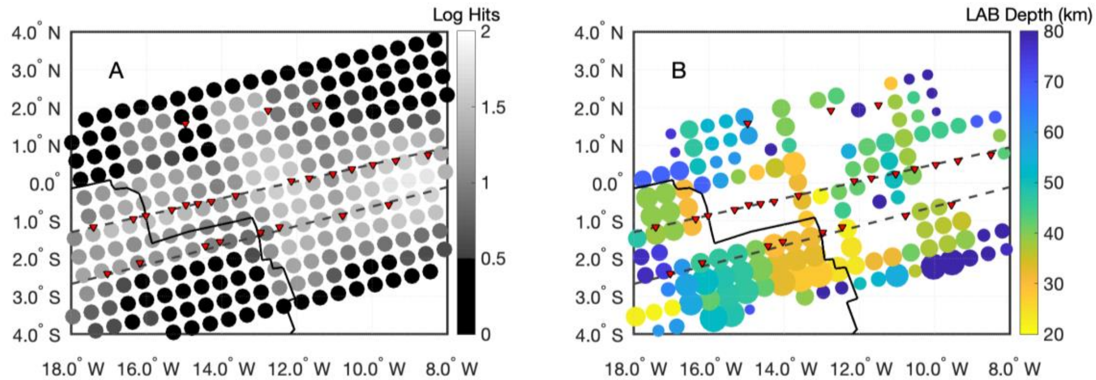

Figure 2

Sp receiver function hit count map and map view of bins with a LAB phase. A) hit count map at 60 km depth. Grey shading indicates the number of waveforms averaged into the bin in Log10(Hits). B) Circles indicate the bin location and color indicates the depth to the LAB. Circle size corresponds to the inverse of error, and bins where the error exceeds the amplitude of the data are not plotted. Black line shows the plate boundary, and dark grey dashed lines show the locations of the two transects. Inverted red triangles show the stations used in this study.

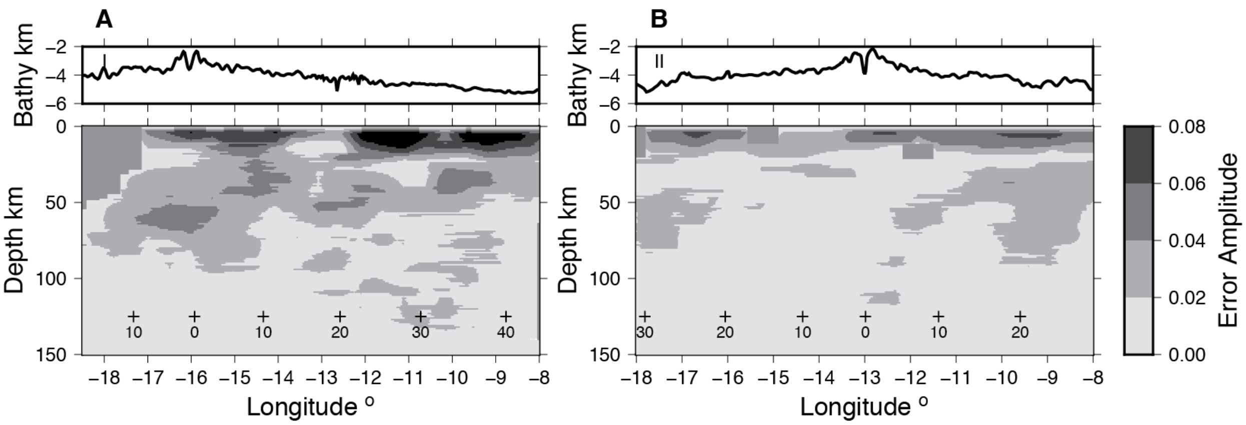

Figure 3

Sp receiver function amplitude error. Here we present 95 % confidence limits on the amplitude of the data stack in transect I the north (A) and transect II in the south (B) as shown in Figure 1.

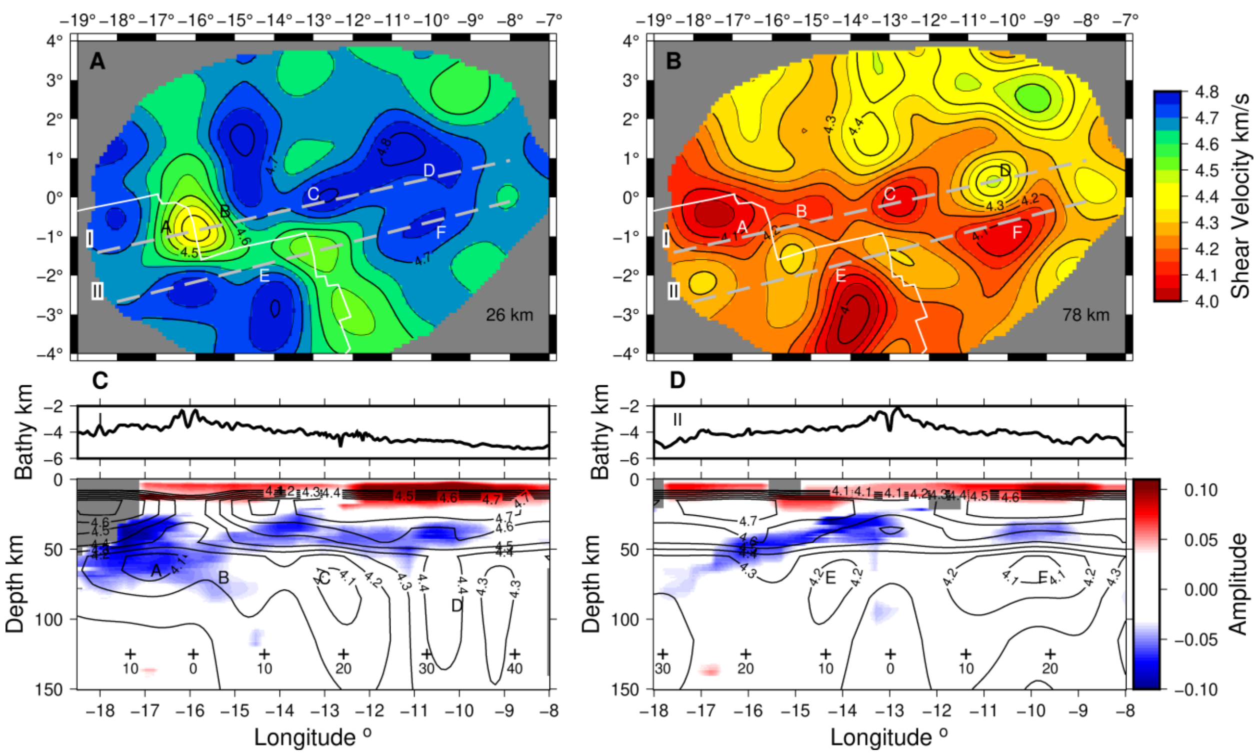

Figure 4

Shear-wave velocity model inferred from inversion of surface waves and Sp receiver functions. Shear-wave velocities from surface waves are shown in map view by colors and contours (red for slow and blue for fast) at A) 26 km depth to illustrate variability owing to plate thickening and B) 78 km depth to illustrate the structure of the punctuated anomalies. White line shows the plate boundary. Dashed grey lines indicate transect locations. Transects through the receiver function and shear-wave models are shown C) and D) for transects I and II. Sp converted phases that result from velocity increases with depth are shown in red and those from decreases with depth are shown in blue. Seafloor bathymetry is plotted above the transects. Grey areas show regions with < 3 hits per bin. Shear-wave velocity from surface waves is shown as black contours with contour labels in km/s. Black crosses show seafloor ages (in Myr) as labeled.

Depths are with respect to the sea surface. Anomaly locations are labelled by capital letters.

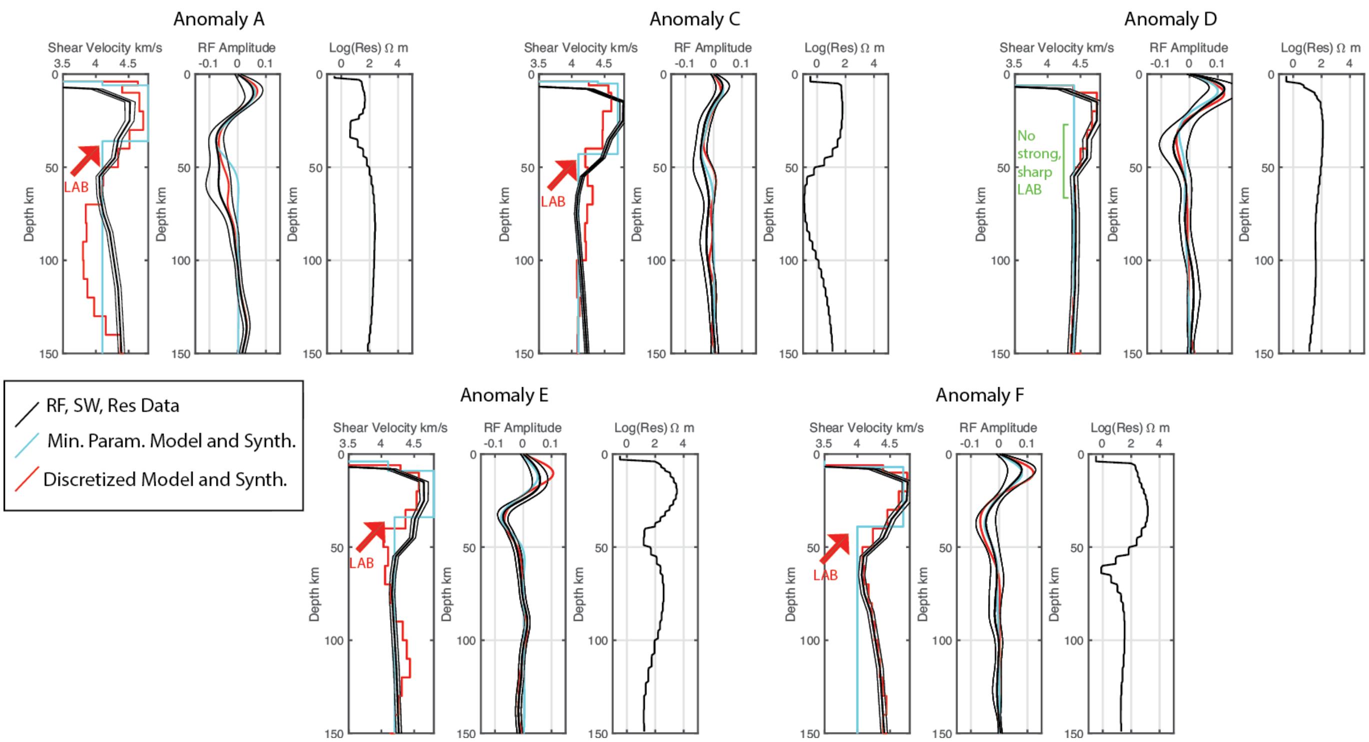

Figure 5

1-D Comparisons of main anomalies. MT imaging (right panels) is compared to the receiver function (RF) data (middle panel, thick black) and 95 % confidence limits (middle panel, thin black) and the shear-wave velocities inferred from surface waves (left panel, thick black) and corresponding 95 % confidence limits (left panel, thin black). Synthetic receiver functions and corresponding shear velocity models from 2 different modelling approaches: a minimum parameterisation (blue) and an over parameterisation (red) are shown in the middle and left panels, respectively. Receiver functions are only sensitive to changes in velocity, although we show possible absolute velocities for comparison with the shear-wave velocities from surface waves. The five major interpreted anomalies as labelled in Fig. 7. Red arrows highlight seismic low velocity zones, significant LAB phases from receiver functions and the depth of the strong sharp drop in velocity in the minimum parameterization model. Green lines show the location where no LAB phase is significant and no slow shear-wave velocity anomaly exists in the shear-wave tomography from surface waves, i.e., the interpreted lithospheric drip.

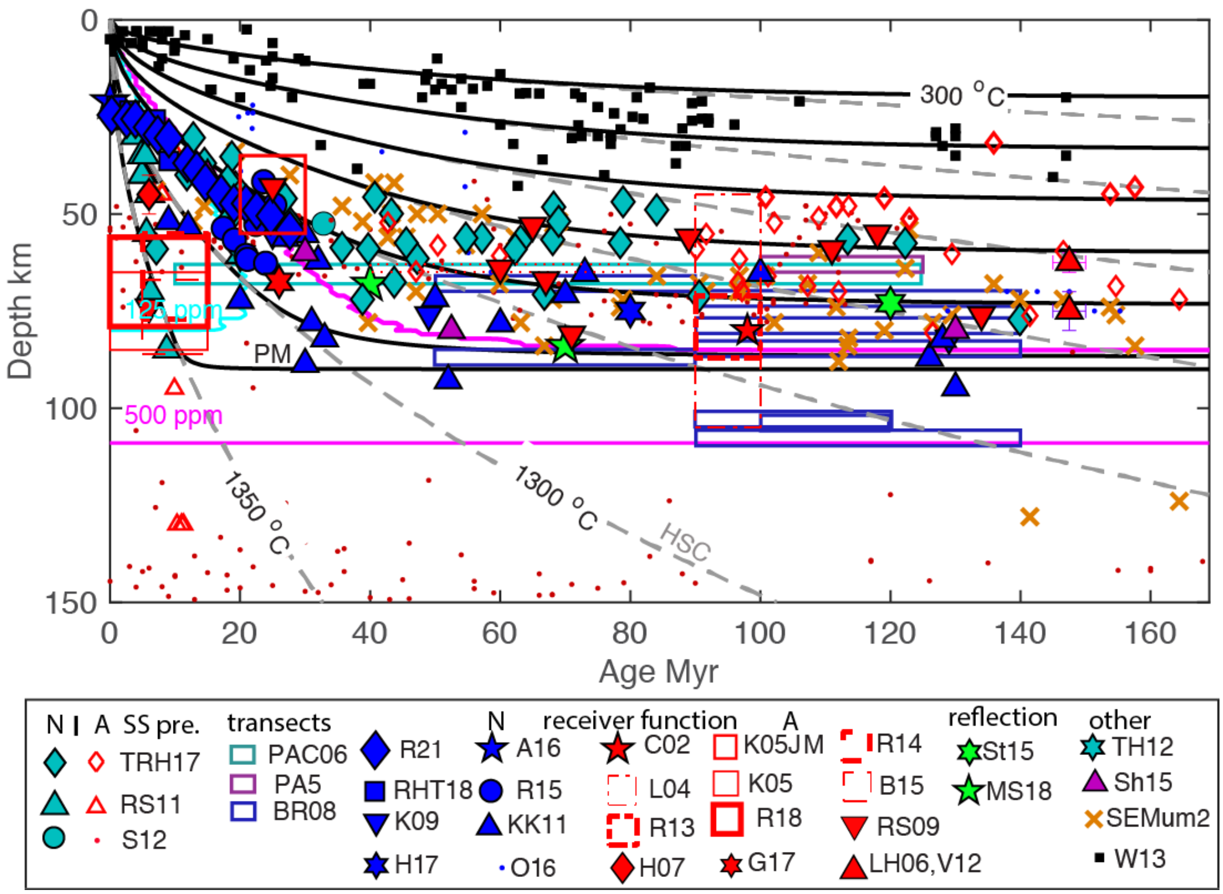

Figure 6

Discontinuity depths from the western side of transect II in the south compared to other observations. Thermal contours are plotted for the half-space cooling model (HSC; grey dashed lines) and the plate model assuming a 90 km thick plate (PM; black lines) at 200 °C interval and also a contour very close to the potential temperature, 1350 °C. The solidi for a mildly hydrated mantle are shown for 125 ppm (cyan) and 500 ppm (pink) water assuming a plate model and 90 km plate thickness. Depths are plotted relative to the seafloor with submarine results corrected from the depth beneath sea surface by the amount listed, if any. SS precursor results from the entire Pacific including (TRH17, RS11, and S12) are sorted into normal lithosphere (N; cyan) and anomalous (A; red) lithosphere affected by hotpots. Transect studies that encompass a range of ages are shown as boxes with fixed thickness (5 km), including: PAC06; PA5 -5, km; and BR08, -4 km. Active source studies (solid green symbols) include MS18, -4 km and St15. Receiver function results from normal (N) ocean lithosphere unaffected by hotspots (solid blue symbols) include this study (R21, -4 km), Cascadia (RHT18, -3 km), offshore California (R15, -3 km), western Pacific (O16), Circum-Pacific (KK11), off-shore Japan (K09), Gloria Fault in the Atlantic (H17); and the Juan de Fuca Ridge (A16). Receiver function studies from ocean island hotspot studies (A, anomalous) are shown as solid red symbols or red boxes where the studies encompass a range of ages or depths, with -5 km depth correction applied to island studies (LH06, V12, K05JM, L04, H07, G17, R14, B15, K05) and the listed amount applied to submarine studies: R13, -4 km and C02. The depths of the minimum velocity in the low-velocity zone beneath the Pacific from surface wave model SEMum2 (-4 km) are shown as orange x's. Oceanic effective elastic thickness estimates are shown by black squares. Depths from a sS precursor result (TH12) is shown by a cyan star and a P_O/S_O result (Sh15) is shown by purple triangles. For a complete set of references please refer to Rychert et al., (2020).

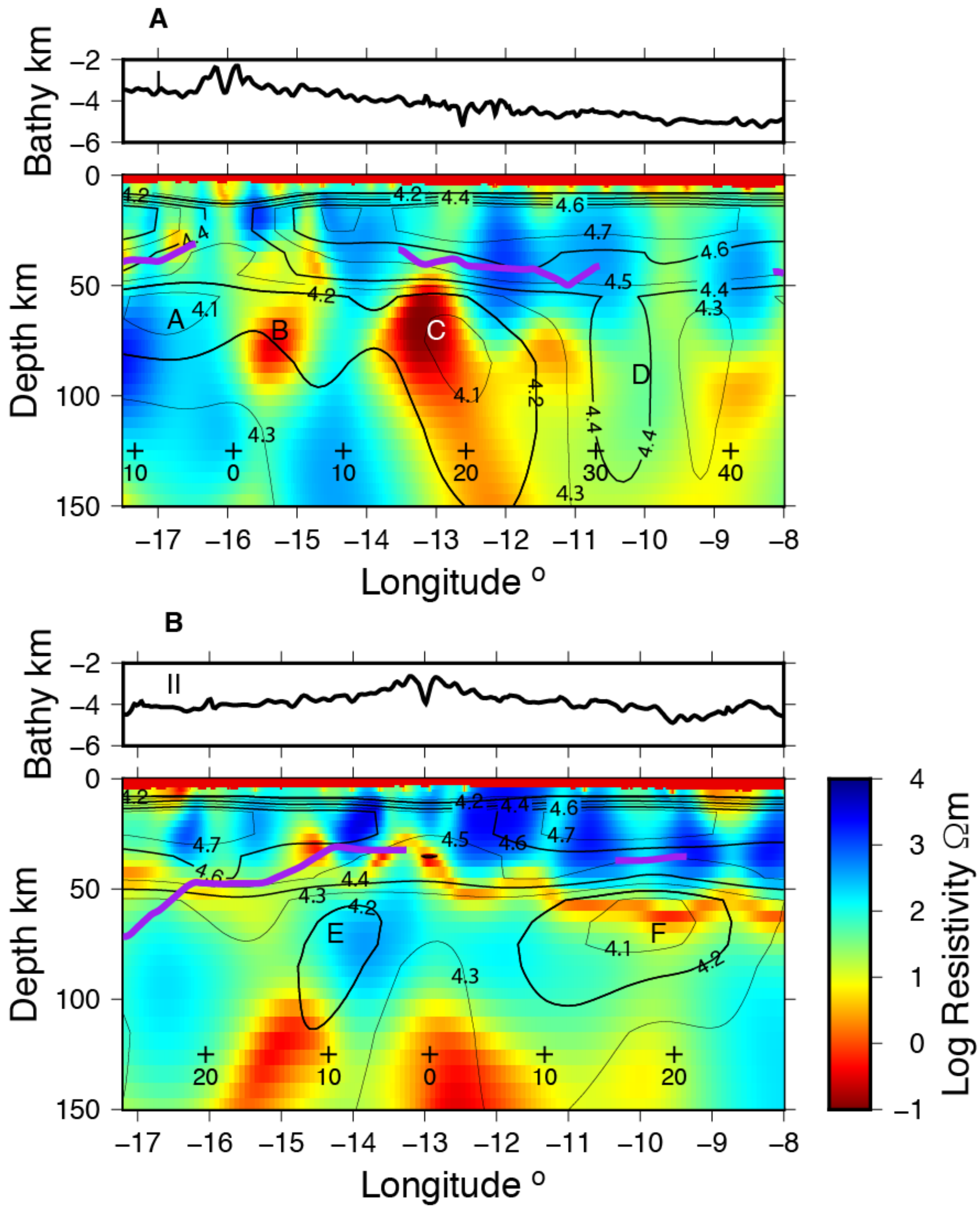

Figure 7

Summary of scientific results. Results from all three methods are presented along the transects (thick black lines, Fig. 1). Background color shows resistivity. Black contours show the shear-wave seismic velocity model from surface waves. Thick purple line shows negative polarity phase from the Sp receiver functions with amplitudes that exceed 95 % confidence limits. Seafloor bathymetry is plotted above the transects. Black crosses show seafloor ages (in Myr) as labeled. Letters indicate anomalies discussed in the text. Depths are with respect to the sea surface.

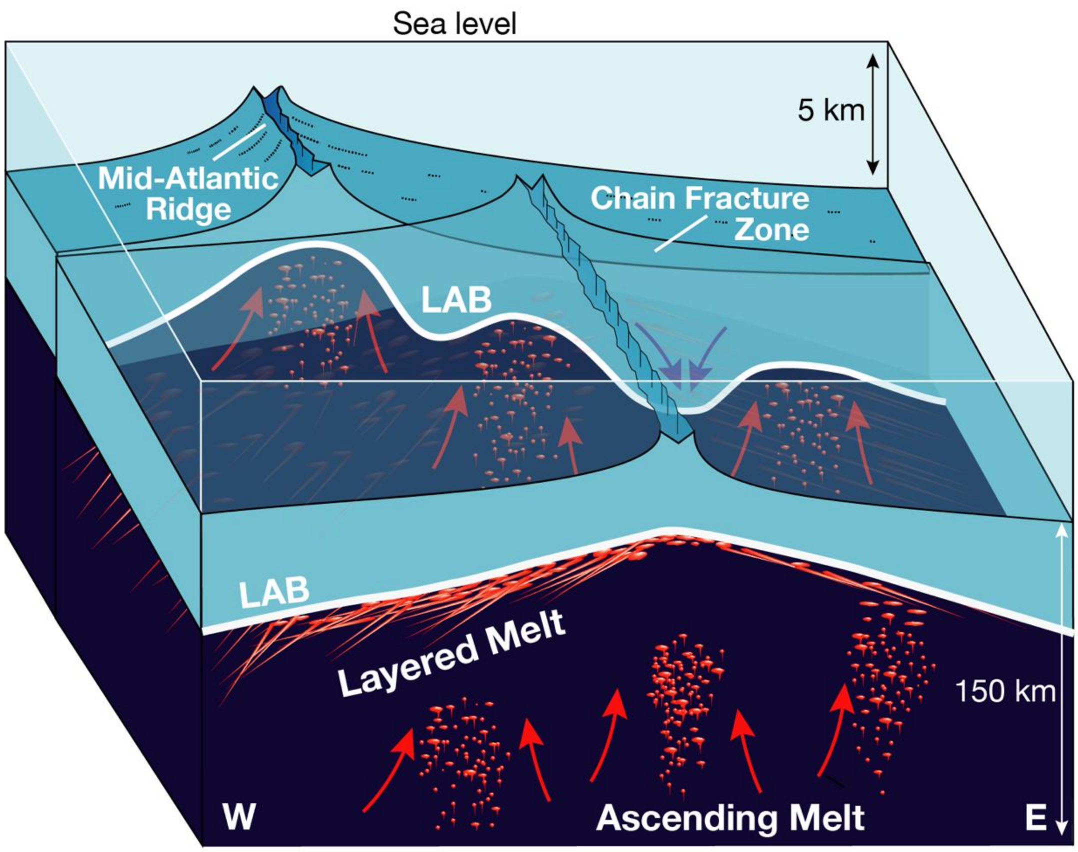

Figure 8

Schematic summary of the interpretation of the results. Front panel shows transect II where melt layers define the base of the plate, with gradually decreasing amounts of melt with depth in the west and a thin melt channel in the east. Partial melt from either chemical heterogeneity and/or small-scale convection ascends from depth. Back panel shows transect I where the age progression of the plate is more complex, possibly owing to alteration by small-scale convection. The LAB is shown as the thick white line.

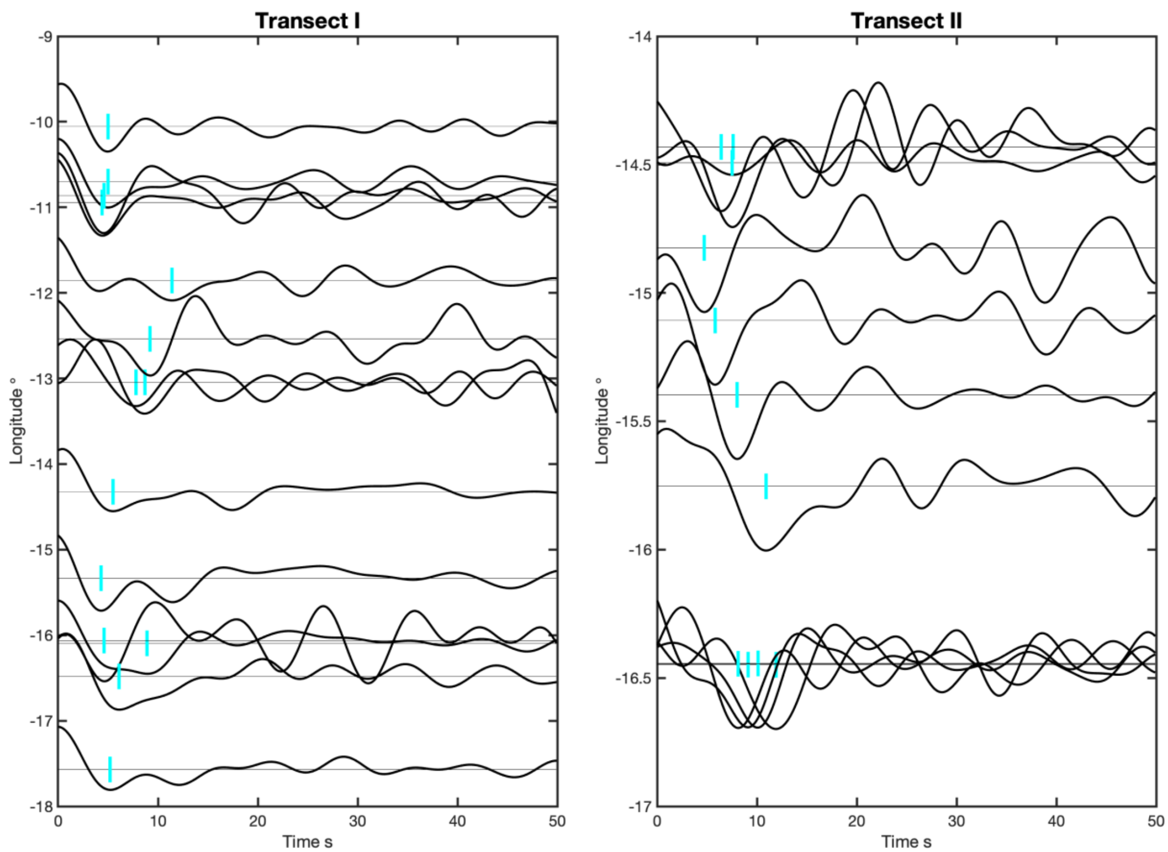

Figure S1

Individual S-to-P receiver function examples. Receiver functions examples with signal to noise ratios > 10 in the raw data that are stacked and highly weighted in the bins located beneath transects I (left) and II (right) are shown. The x-axes correspond to the differential time before the S-wave. The y-axes correspond to the longitude of the conversion point. These receiver functions are converted at any depth beneath the transect. In the final model these examples are also stacked with many more seismograms of similar quality. Therefore, a 1-to-1 correlation with the models presented in Figure 1 and 4 is not expected. A positive phase is imaged at < 5 s that is related to the Moho. It is shallower in some cases owing to interference with internal Moho discontinuities. In addition, a negative discontinuity is imaged in transect II (marked by cyan lines) with increasing differential time towards the west, corresponding to the interpreted thickening plate. In transect I greater complexity is imaged, and in some cases two negative discontinuities exist, potentially related to complex topography. Overall, the figure demonstrates what goes into the stacks. Other phases are present besides the Moho-related phase and the LAB in some receiver functions. Additional phases besides the Moho-related phase and the LAB are likely related to noise because they stack out in the final model. The figure demonstrates that the Moho and/or Moho-related phase and LAB phases exist in the raw receiver functions and do not correspond to wrongly interpreted noise. Phases that are not significantly different from zero according to formal error are not plotted or interpreted in Fig. 7.

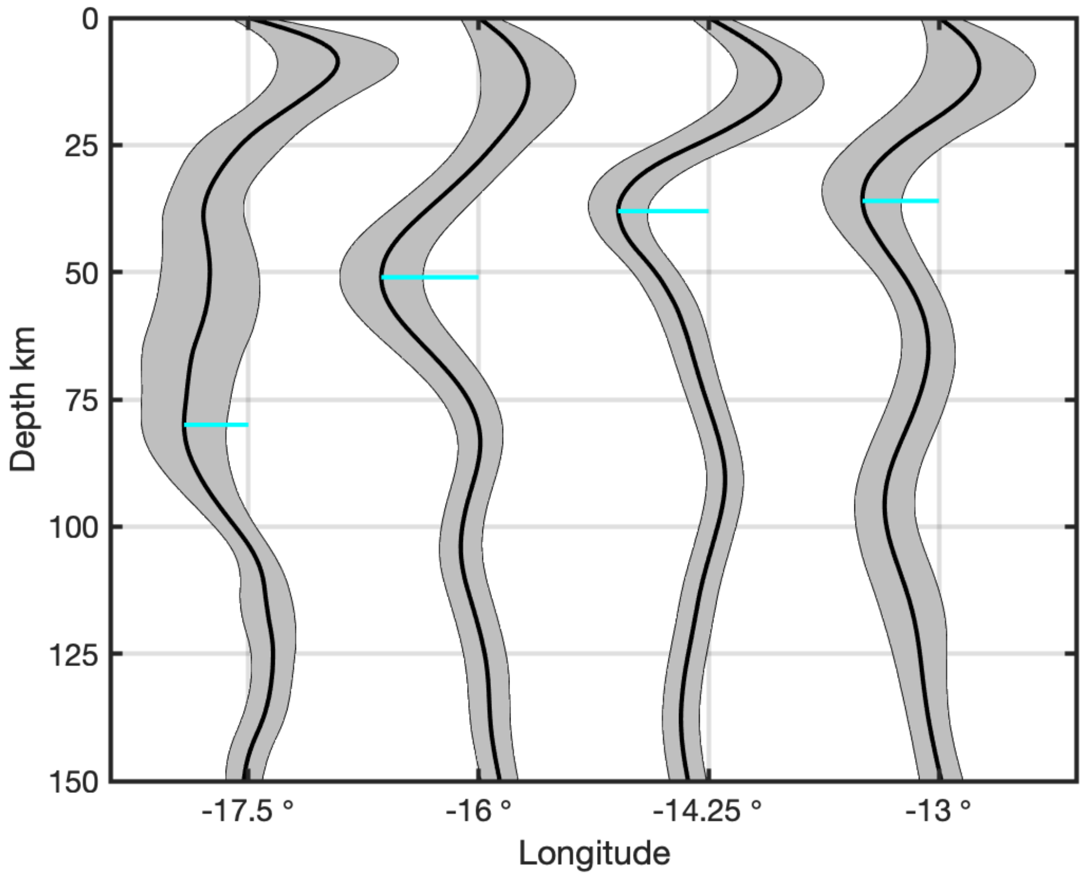

Figure S2

Vertical receiver functions from the stacked model from the western half of transect II in the south. Thick black lines show the receiver functions and grey region show the 95 % confidence limits. Cyan lines show the depths of the interpreted LAB phases.

REFERENCES CITED

Agius, M., Rychert, C.A., Harmon, N., Kendall, J.M., Tharimena, S., 2021. Transition zone thinning beneath the Mid-Atlantic Ridge suggests whole mantle convection. Nature 589, doi:10.1038/s41586-020-03139-x.

Agius, M.R., Harmon, N., Rychert, C.A., Tharimena, S., Kendall, J.M., 2018. Sediment characterization at the equatorial Mid-Atlantic Ridge from P-to-S teleseismic phase conversions recorded on the PI-LAB Experiment. Geophysical Research Letters 45, doi:10.1029/2018gl080565.

Baba, K., Chave, A.D., Evans, R.L., Hirth, G., Mackie, R.L., 2006. Mantle dynamics beneath the East Pacific Rise at 17 degrees S: Insights from the Mantle Electromagnetic and Tomography (MELT) experiment. J. Geophys. Res. 111, doi:10.1029/2004JB003598.

Beghein, C., Yuan, K.Q., Schmerr, N., Xing, Z., 2014. Changes in seismic anisotropy shed light on the nature of the Gutenberg Discontinuity. Science 343, doi:10.1126/science.1246724.

Bell, S., Ruan, Y.Y., Forsyth, D.W., 2016. Ridge asymmetry and deep aqueous alteration at the trench observed from Rayleigh wave tomography of the Juan de Fuca plate. J. Geophys. Res. 121, doi:10.1002/2016JB012990.

Buck, W.R., Parmentier, E.M., 1986. Convection beneath young oceanic lithosphere - Implications for thermal structure and gravity. J. Geophys. Res. 91, doi:10.1029/JB091iB02p01961.

Burgos, G., Montagner, J.P., Beucler, E., Capdeville, Y., Mocquet, A., Drilleau, M., 2014. Oceanic lithosphere-asthenosphere boundary from surface wave dispersion data. J Geophys Res-Sol Ea 119, doi:10.1002/2013jb010528.

Cline, C.J., Faul, U.H., David, E.C., Berry, A.J., Jackson, I., 2018. Redox-influenced seismic properties of uppermantle olivine. Nature 555, doi:10.1038/nature25764.

Coli, L., Stotz, I., Bunge, H.P., Smethurst, M., Clark, S., Iaffaldano, G., Tassara, A., Guillocheau, F., Bianchi, M.C., 2014. Rapid South Atlantic spreading changes and coeval vertical motion in surrounding continents: Evidence for temporal changes of pressure-driven upper mantle flow. Tectonics 32, doi:10.1002/2014TC003612.

Conder, J.A., Forsyth, D.W., Parmentier, E.M., 2002. Asthenospheric flow and asymmetry of the East Pacific Rise, MELT area. J. Geophys. Res. 107, doi:10.1029/2001JB000807.

Dziewonski, A.M., Anderson, D.L., 1981. Preliminary reference Earth model. Phys. Earth Planet. Inter. 25

Fischer, K., Rychert, C., Dalton, C., Miller, M., Beghein, C., Schutt, D., 2020. A comparison of oceanic and continental mantle lithosphere. Phys Earth Planet In 309, doi:10.1016/j.pepi.2020.106600.

Forsyth, D.W., Scheirer, D.S., Webb, S.C., Dorman, L.M., Orcutt, J.A., Harding, A.J., Blackman, D.K., Morgan, J.P., Detrick, R.S., Shen, Y., Wolfe, C.J., Canales, J.P., Toomey, D.R., Sheehan, A.F., Solomon, S.C., Wilcock, W.S.D., Team, M.S., 1998. Imaging the deep seismic structure beneath a mid-ocean ridge: The MELT experiment. Science 280, doi:10.1126/science.280.5367.1215.

French, S.W., Lekic, V., Romanowicz, B., 2013. Waveform Tomography Reveals Channeled Flow at the Base of the Oceanic Asthenosphere. Science 342, doi:10.1126/science.1241514.

Gaherty, J.B., Jordan, T.H., Gee, L.S., 1996. Seismic structure of the upper mantle in a central Pacific corridor. J. Geophys. Res. 101, doi:10.1029/96JB01882.

Harmon, N., Forsyth, D.W., Weeraratne, D.S., 2009. Thickening of young Pacific lithosphere from high-resolution Rayleigh wave tomography: A test of the conductive cooling model. Earth Planet. Sci. Lett. 278, doi:10.1016/J.Epsl.2008.11.025.

Harmon, N., Forsyth, D.W., Weeraratne, D.S., Yang, Y.J., Webb, S.C., 2011. Mantle heterogeneity and off axis volcanism on young Pacific lithosphere. Earth Planet. Sci. Lett. 311, doi:10.1016/J.Epsl.2011.09.038.

Harmon, N., Rychert, C., Kendall, J., Tharimena, S., Bogiatzis, P., Agius, M., 2020. Evolution of the oceanic lithosphere in the equatorial Atlantic from Rayleigh Wave tomography, evidence for small-scale convection from the PI-LAB experiment. Geochem Geophy Geosy Geochem Geophy Geosy, doi:10.1029/2020GC009174.

Harmon, N., Rychert, C.A., Agius, M.R., Tharimena, S., Le Bas, T.P., Kendall, J.M., Constable, S., 2018. Marine geophysical investigation of the Chain Fracture Zone in the equatorial Atlantic from the PI-LAB Experiment. J. Geophys. Res. 123, doi:10.1029/2018jb015982.
Helffrich, G., 2006. Extended-time multitaper frequency domain cross-correlation receiver-function estimation. B Seismol Soc Am 96, doi:10.1785/0120050098.
Hirth, G., Kohlstedt, D.L., 1995. Experimental constraints on the dynamics of the partially molten upper-mantle .2. Deformation in the dislocation creep regime. J. Geophys. Res. 100, doi:10.1029/94JB02128.
Jackson, I., Faul, U.H., 2010. Grainsize-sensitive viscoelastic relaxation in olivine: Towards a robust laboratory-based model for seismological application. Phys. Earth Plan. Int. 183, doi:10.1016/J.Pepi.2010.09.005.
Jackson, I., Faul, U.H., Fitz Gerald, J.D., Morris, S.J.S., 2006. Contrasting viscoelastic behavior of melt-free and melt-bearing olivine: Implications for the nature of grain-boundary sliding. Materials Science and Engineering a-Structural Materials Properties Microstructure and Processing 442, doi:10.1016/J.Msea.2006.01.136.
Johansen, S.E., Panzner, M., Mittet, R., Amundsen, H.E.F., Lim, A., Vik, E., Landrø, M., Arntsen, B., 2019. Deep electrical imaging of the ultraslow-spreading Mohns Ridge. Nature 567, doi:10.1038/s41586-019-1010-0.
Karato, S.I., Olugboji, T., Park, J., 2015. Mechanisms and geologic significance of the mid-lithosphere discontinuity in the continents. Nature Geoscience 8, doi:10.1038/Ngeo2462.
Katz, R., 2010. Porosity-driven convection and asymmetry beneath mid-ocean ridges. Geochem. Geophys. Geosyst. 11
Kawakatsu, H., Kumar, P., Takei, Y., Shinohara, M., Kanazawa, T., Araki, E., Suyehiro, K., 2009. Seismic evidence for sharp lithosphere-asthenosphere boundaries of oceanic plates. Science 324, doi:10.1126/science.1169499.
Key, K., Constable, S., Liu, L., Pommier, A., 2013. Electrical image of passive mantle upwelling beneath the northern East Pacific Rise. Nature 495, doi:10.1038/nature11932.
Lekic, V., Fischer, K.M., 2017. Interpreting spatially stacked Sp receiver functions. Geophys. J. Int. 210, doi:10.1093/gji/ggx206.
Mehouachi, F., Singh, S., 2018. Water-rich sublithospheric melt channel in the equatorial Atlantic Ocean. Nat. Geosci. 11, doi:10.1038/s41561-017-0034-z.
Morgan, J.P., Parmentier, E.M., Lin, J., 1987. Mechanisms for the origin of midocean ridge axial topography - Implications for the thermal and mechanical structure of accreting plate boundaries. J. Geophys. Res. 92, doi:10.1029/JB092iB12p12823.
Muller, R.D., Sdrolias, M., Gaina, C., Roest, W.R., 2008. Age, spreading rates, and spreading asymmetry of the world's ocean crust. Geochem. Geophys. Geosyst. 9, doi:10.1029/2007gc001743.
Naif, S., Key, K., Constable, S., Evans, R.L., 2013. Melt-rich channel observed at the lithosphere-asthenosphere boundary. Nature 495, doi:10.1038/nature11939.
Parker, R.L., Whaler, K.A., 1981. Numerical methods for establishing solutions to the inverse problem of electromagnetic induction. . J. Geophys. Res. 86, doi:10.1029/JB086iB10p09574.
Parmentier, E.M., Morgan, J.P., 1990. Spreading Rate Dependence of 3-Dimensional Structure in Oceanic Spreading Centers. Nature 348, doi:10.1038/348325a0.
Parsons, B., Sclater, J.G., 1977. Analysis of Variation of Ocean-Floor Bathymetry and Heat-Flow with Age. J. Geophys. Res. 82, doi:10.1029/JB082i005p00803.

Richter, F.M., 1973. Convection and large-scale circulation of mantle. J. Geophys. Res. 78, doi:10.1029/JB078i035p08735.
Rychert, C.A., Hammond, J.O.S., Harmon, N., Kendall, J.M., Keir, D., Ebinger, C., Bastow, I.D., Ayele, A., Belachew, M., Stuart, G., 2012. Volcanism in the Afar Rift sustained by decompression melting with minimal plume influence. Nat Geosci 5, doi:10.1038/Ngeo1455.
Rychert, C.A., Harmon, N., 2018. Predictions and observations for the oceanic lithosphere from S-to-P receiver functions and SS precursors. Geophys. Res. Lett. 45, doi:10.1029/2018gl077675.
Rychert, C.A., Harmon, N., Constable, S., Wang, S., 2020. The Nature of the Lithosphere-Asthenosphere Boundary. J. Geophys. Res., doi:10.1029/2018JB016463.
Rychert, C.A., Harmon, N., Tharimena, S., 2018a. Scattered wave imaging of the oceanic plate in Cascadia. Sci Adv Sci Adv 4, doi:10.1126/sciadv.aao1908.
Rychert, C.A., Harmon, N., Tharimena, S., 2018b. Seismic Imaging of the Base of the Ocean Plates, in: Yuan, H. (Ed.), Lithospheric Discontinuities. AGU Monographs, Washington DC, pp. 71-87, doi:10.1002/9781119249740.ch4.
Rychert, C.A., Shearer, P.M., 2009. A Global View of the Lithosphere-Asthenosphere Boundary. Science 324, doi:10.1126/science.1169754.
Saikia, U., Rychert, C.A., Harmon, N., Kendall, J.M., 2020. Sediment Structure at the Equatorial Mid-Atlantic Ridge Constrained by Seafloor Admittance using data from the PI-LAB experiment. Marine Geophys. Res., doi:10.1029/2018GL080565.
Saikia, U., Rychert, C.A., Harmon, N., Kendall, J.M., 2021. Upper mantle anisotropic shear velocity structure at the equatorial Mid-Atlantic Ridge constrained by Rayleigh wave group velocity analysis from the PI-LAB experiment Geochem Geophy Geosy Geochem Geophy Geosy, doi:10.1029/2020GC009495
Shibutani, T., Ueno, T., Hirahara, K., 2008. Improvement in the extended-time multitaper receiver function estimation technique. B Seismol Soc Am 98, doi:10.1785/0120070226.
Sim, S.J., Spiegelman, M., Stegman, D.R., Wilson, C., 2020. The influence of spreading rate and permeability on melt focusing beneath mid-ocean ridges. Phys. Earth & Planet. Int. 304, doi:10.1016/j.pepi.2020.106486.
Sparks, D., Parmentier, E., 1991. Melt extraction from the mantle beneath spreading centers. Earth & Planet. Sci. Lett. 105, doi:10.1016/0012-821X(91)90178-K.
Stern, T.A., Henrys, S.A., Okaya, D., Louie, J.N., Savage, M.K., Lamb, S., Sato, H., Sutherland, R., Iwasaki, T., 2015. A seismic reflection image for the base of a tectonic plate. Nature 518, doi:10.1038/nature14146.
Tan, Y., Helmberger, D.V., 2007. Trans-Pacific upper mantle shear velocity structure. J. Geophys. Res. 112, doi:10.1029/2006JB004853.
Tharimena, S., Rychert, C., Harmon, N., White, P., 2017. Imaging Pacific lithosphere seismic discontinuitiesInsights from SS precursor modeling. J. Geophys. Res. 122, doi:10.1002/2016jb013526.
Thybo, H., 2006. The heterogeneous upper mantle low velocity zone. Tectonophysics Tectonophysics 416, doi:10.1016/j.tecto.2005.11.021.
Toomey, D.R., Wilcock, W.S.D., Conder, J.A., Forsyth, D.W., Blundy, J.D., Parmentier, E.M., Hammond, W.C., 2002. Asymmetric mantle dynamics in the MELT region of the East Pacific Rise. Earth Planet. Sci. Lett. 200, doi:10.1016/S0012-821X(02)00655-6.
Wang, S., Constable, S., Rychert, C., Harmon, N., 2020. A lithosphere-asthenosphere boundary and partial melt estimated using marine magnetotelluric data at the central Middle Atlantic Ridge. doi:10.1029/2020GC009177.

Yamauchi, H., Takei, Y., 2016. Polycrystal anelasticity at near-solidus temperatures. J. Geophys. Res. 121, doi:10.1002/2016jb013316.

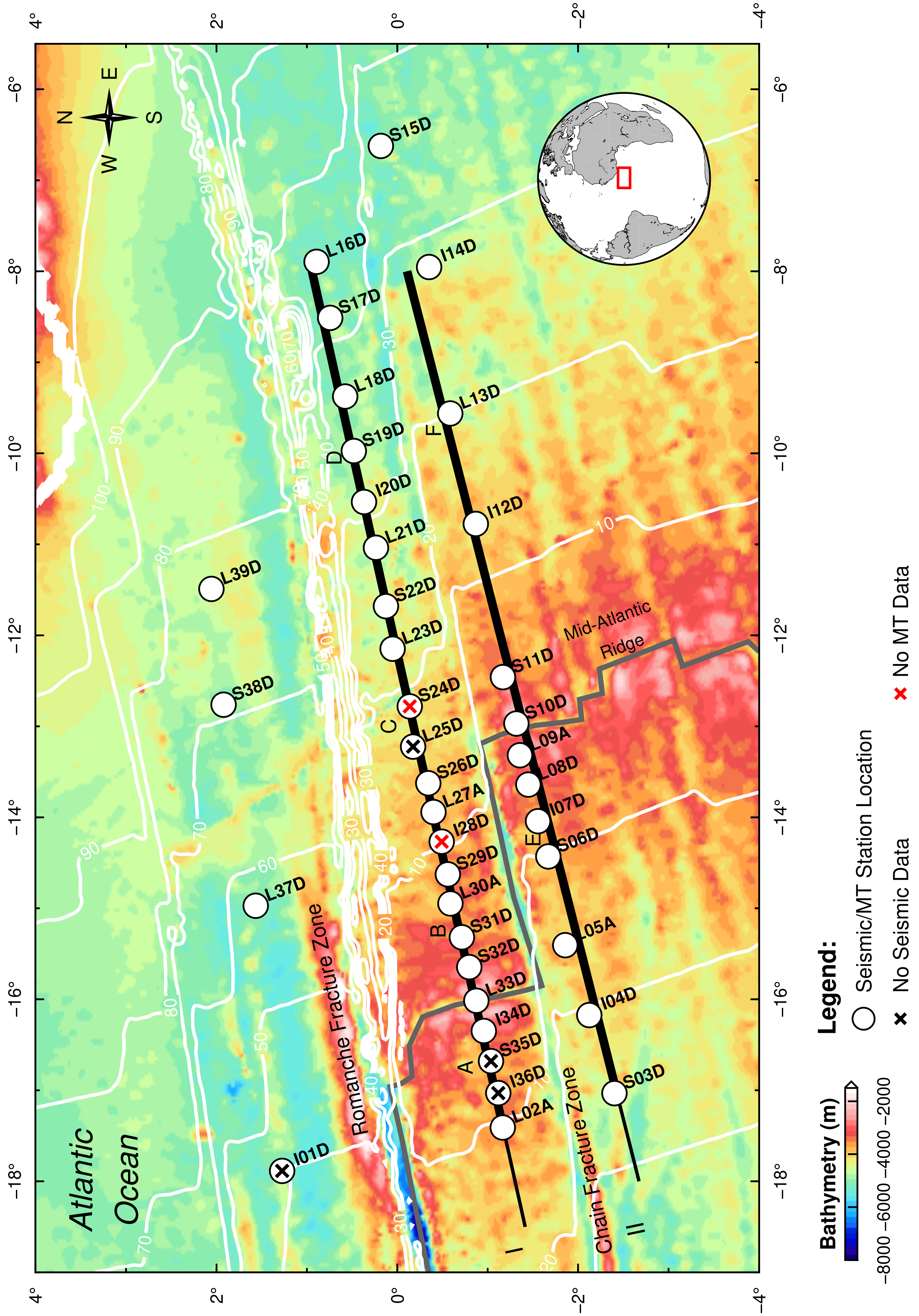
Atlantic
Ocean
Romanche Fracture Zone
Chain Fracture Zone
Mid-Atlantic
Ridge
N
E
S
W
S15D
L16D
S17D
L18D
S19D
I20D
L21D
S22D
L23D
S24D
L25D
S26D
L27A
I28D
S29D
L30A
S31D
S32D
L33D
I34D
S35D
I36D
L02A
I14D
L13D
I12D
S11D
S10D
L09A
L08D
I07D
S06D
L05A
I04D
S03D
L39D
S38D
L37D
I01D
A
B
C
D
E
F
I
II
Legend:
Seismic/MT Station Location
No Seismic Data
No MT Data
Bathymetry (m)
−8000 −6000 −4000 −2000

Figure 2

Click here to access/download;Figure;Figure2.pdf

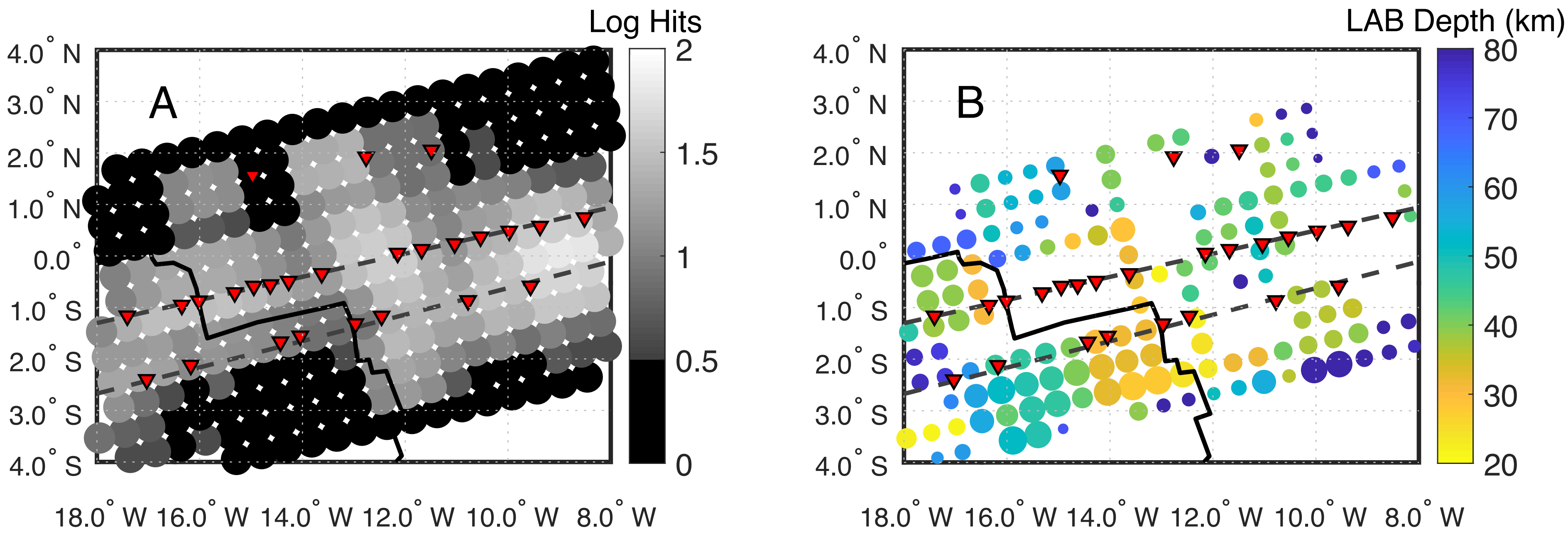

Figure 3 Click here to access/download;Figure;Figure3.pdf

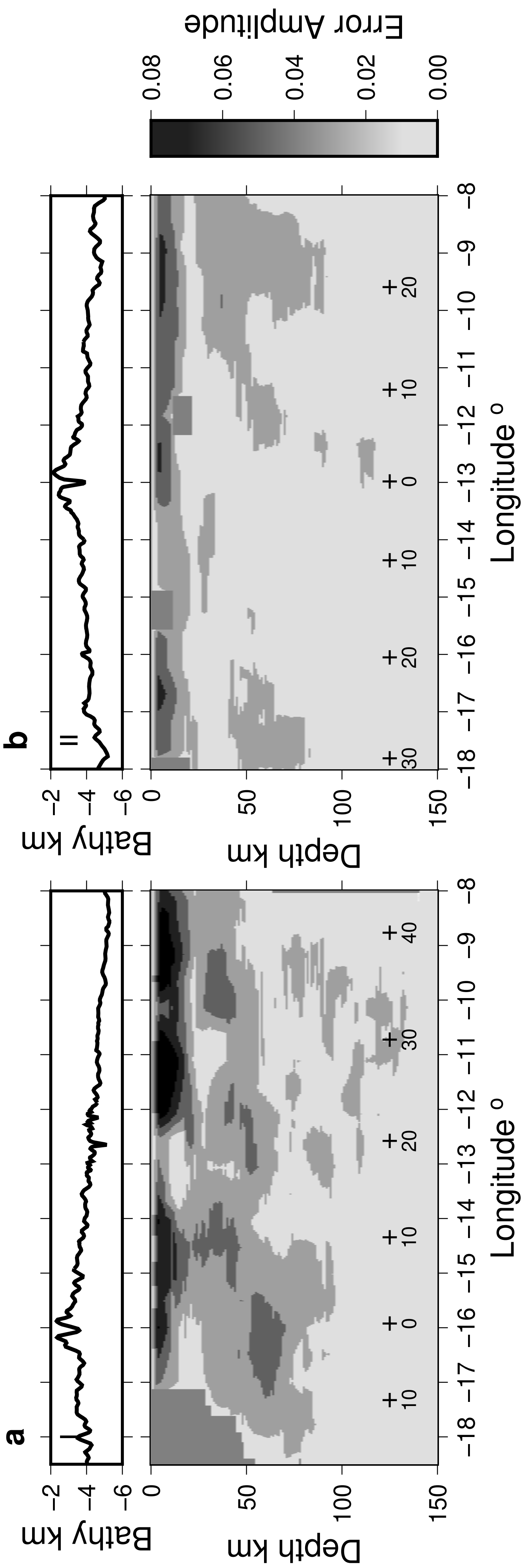

Figure 4

Click here to access/download;Figure;Figure4.pdf

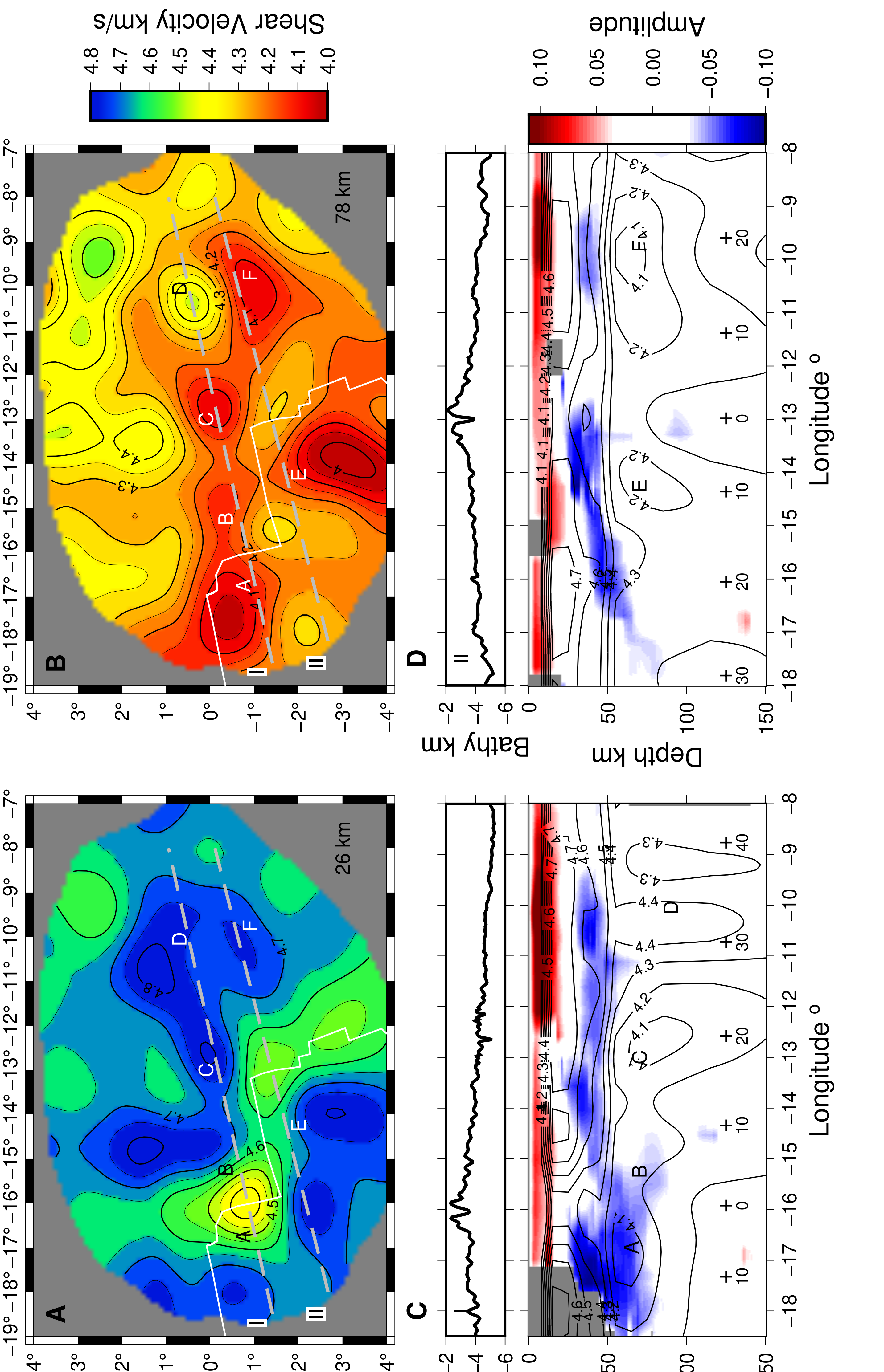

Figure 5

Click here to access/download;Figure;Figure5.pdf

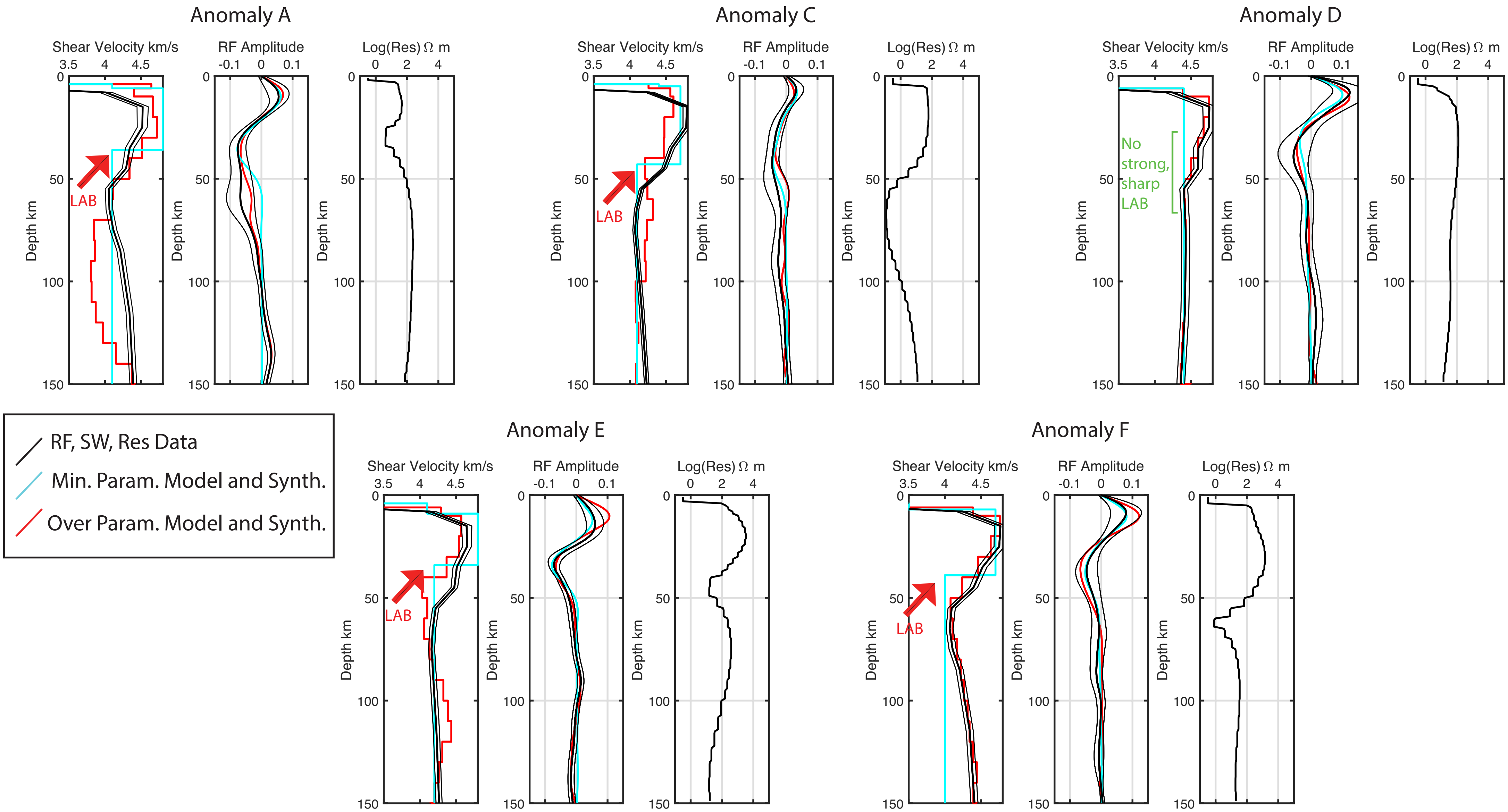

Figure 6

Click here to access/download;Figure;Figure6.pdf

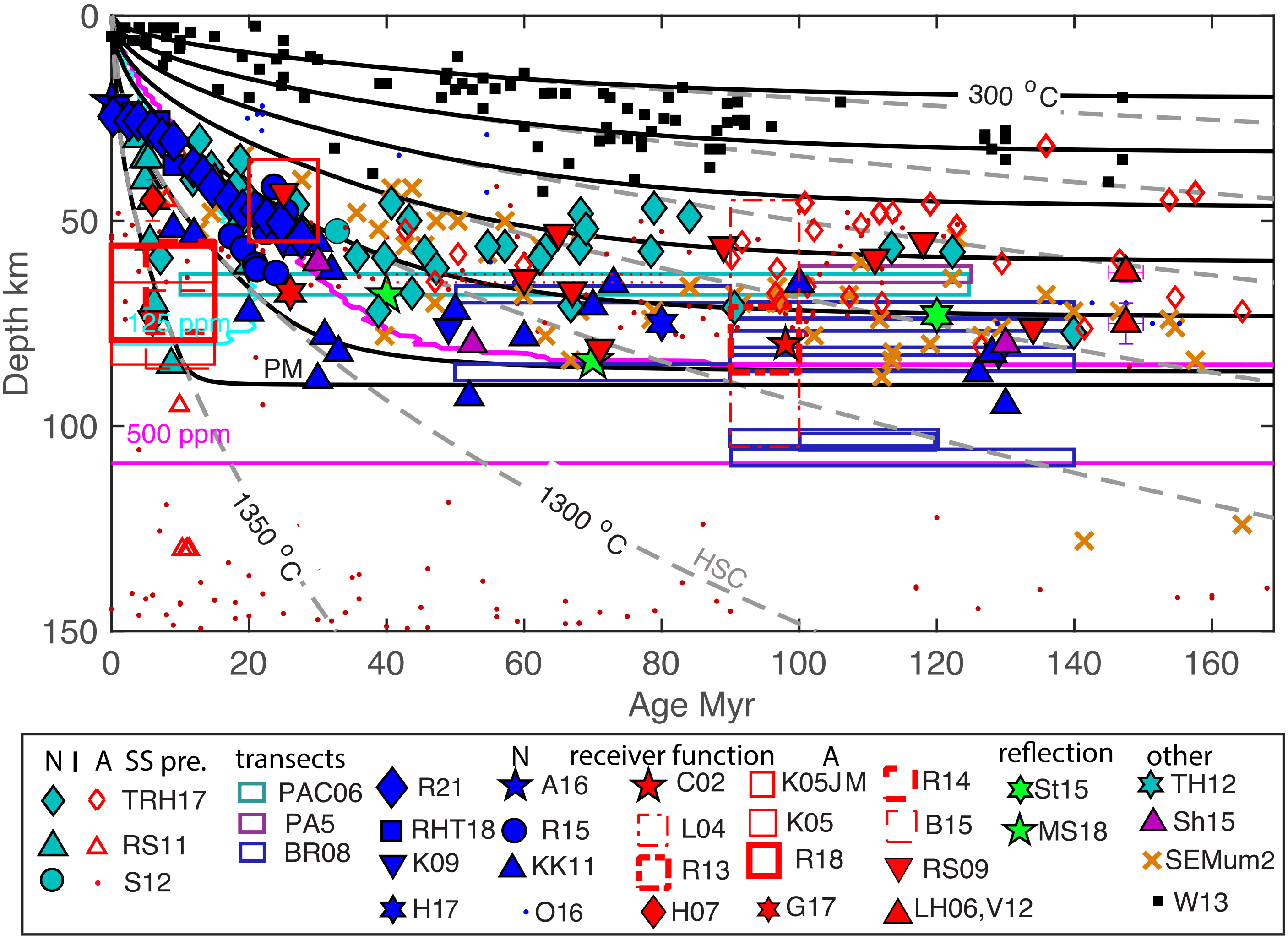

Figure 7

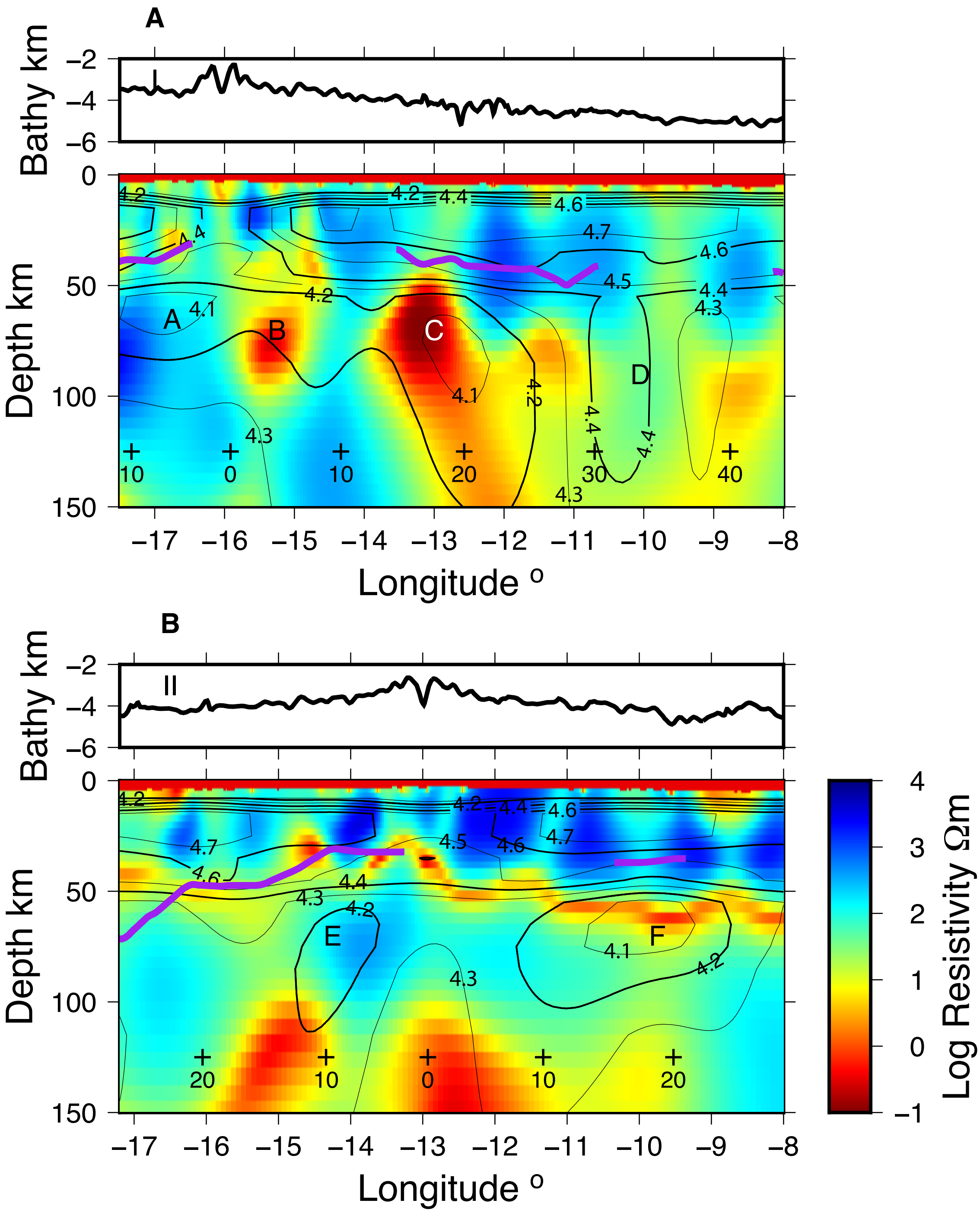

A
Bathy km
−2
−4
−6
0
50
100
150
Depth km
4.2
4.4
4.6
4.7
4.5
4.3
4.1
A
B
C
D
10
0
10
20
30
40
−17
−16
−15
−14
−13
−12
−11
−10
−9
−8
Longitude o
B
II
Bathy km
Depth km
E
F
20
10
0
10
20
Longitude o
Log Resistivity Ωm
4
3
2
1
0
−1

Figure S1

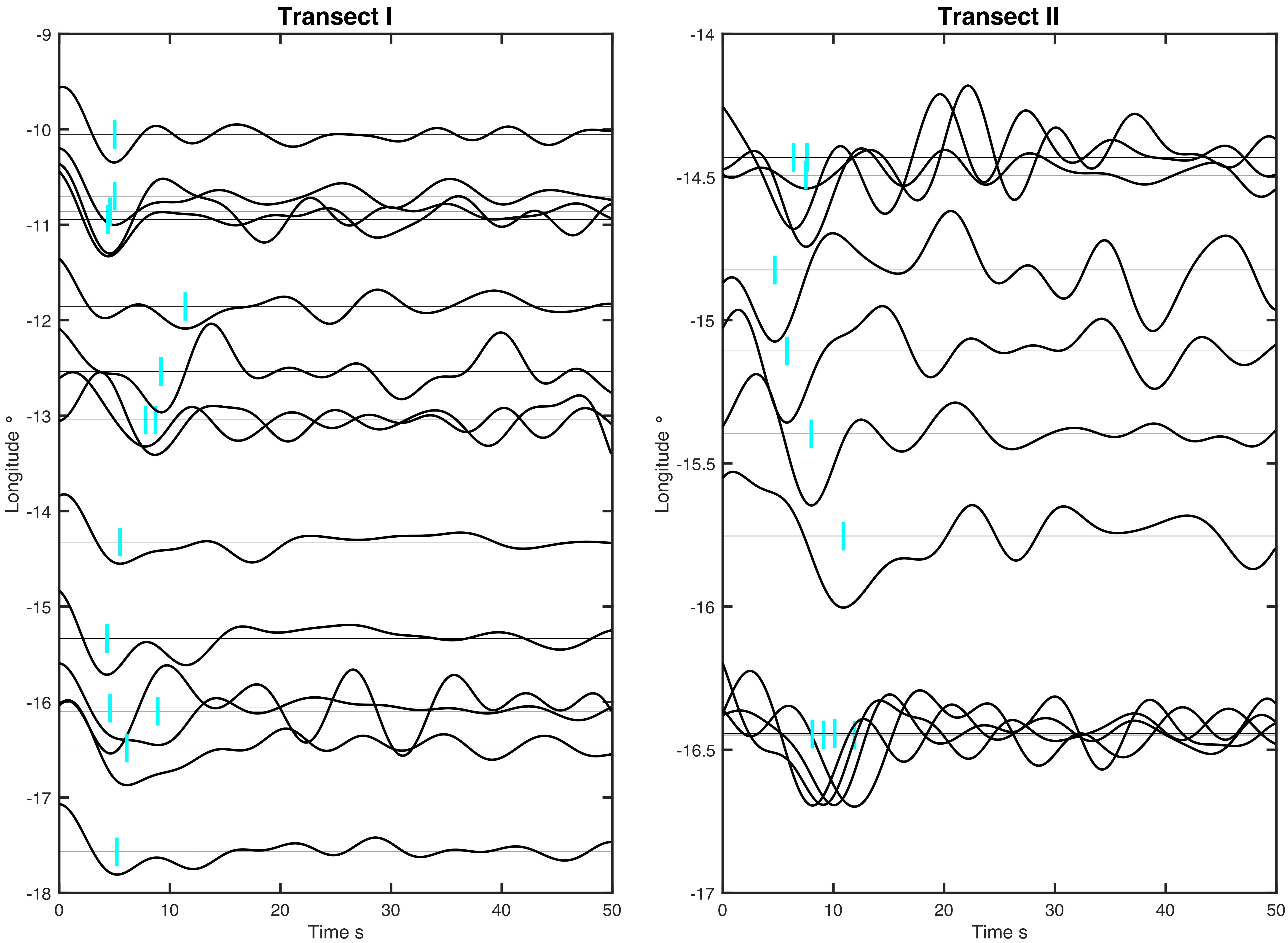
Transect I
Transect II
Longitude °
Longitude °
Time s
Time s
-9
-10
-11
-12
-13
-14
-15
-16
-17
-18
-14.5
-15.5
-16.5
0
10
20
30
40
50

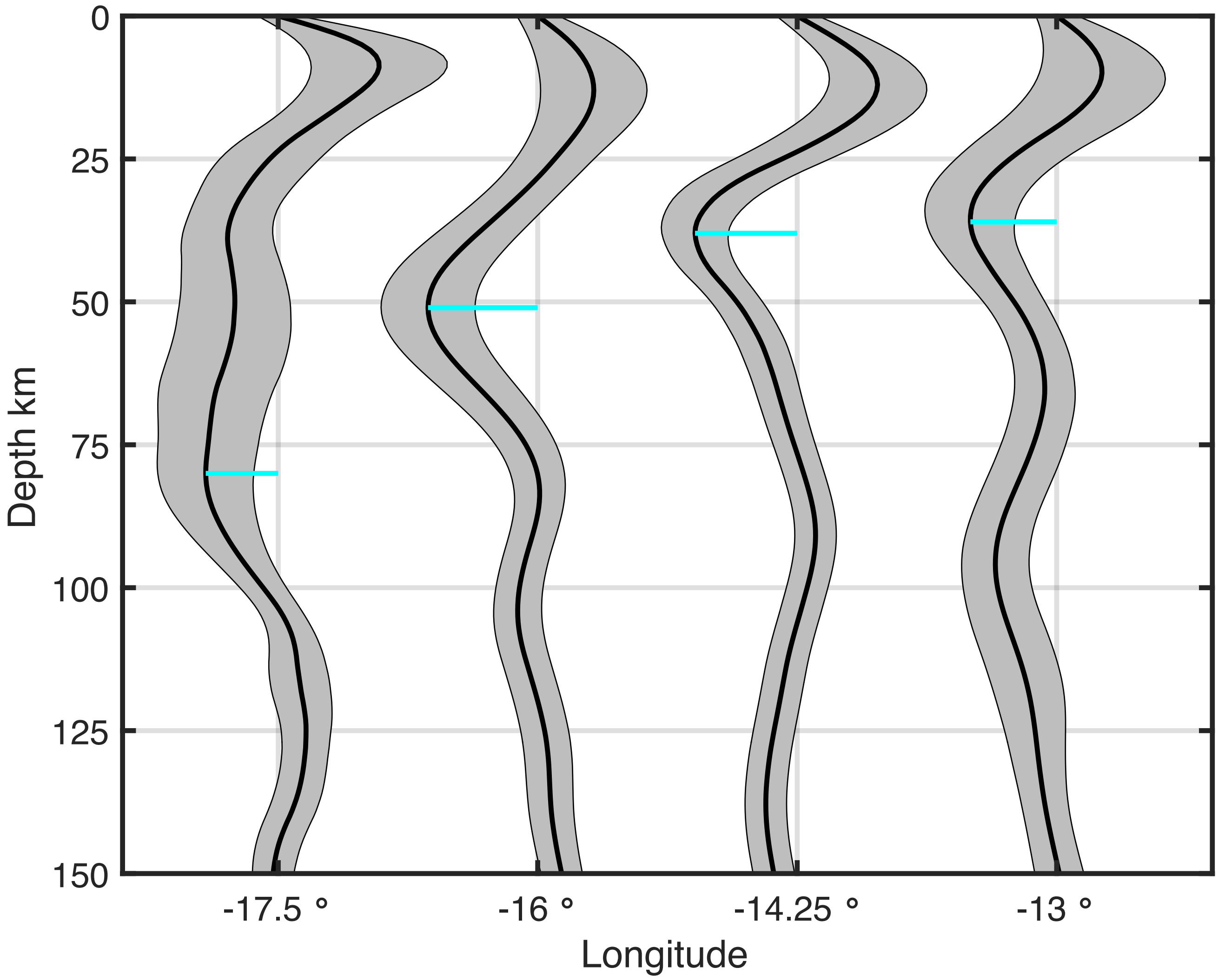
0
25
50
75
100
125
150
Depth km
-17.5 °
-16 °
-14.25 °
-13 °
Longitude

Catherine Rychert & Nicholas Harmon: Conceptualization, Validation, Formal Analysis, Methodology, Software, Resources, Data Curation, Writing - Review & Editing, Visualization, Supervision, Project Administration **Sai Tharimena:** Validation, Formal Analysis, Data Curation, Writing - Review & Editing **Shunguo Wang:** Validation, Formal Analysis, Writing - Review & Editing **Steven Constable:** Conceptualization, Validation, Formal Analysis, Writing - Review & Editing, Supervision, Project Administration **Mike Kendall:** Conceptualization, Data Curation, Writing - Review & Editing, Supervision **Petros Bogiatzis, Matthew Agius, and David Schlaphorst:** Data Curation, Writing - Review & Editing